Developing HydroKinetic Wingtip Devices

John Brindley, Jesse Shull, Ian Gagnon

April 25, 2014

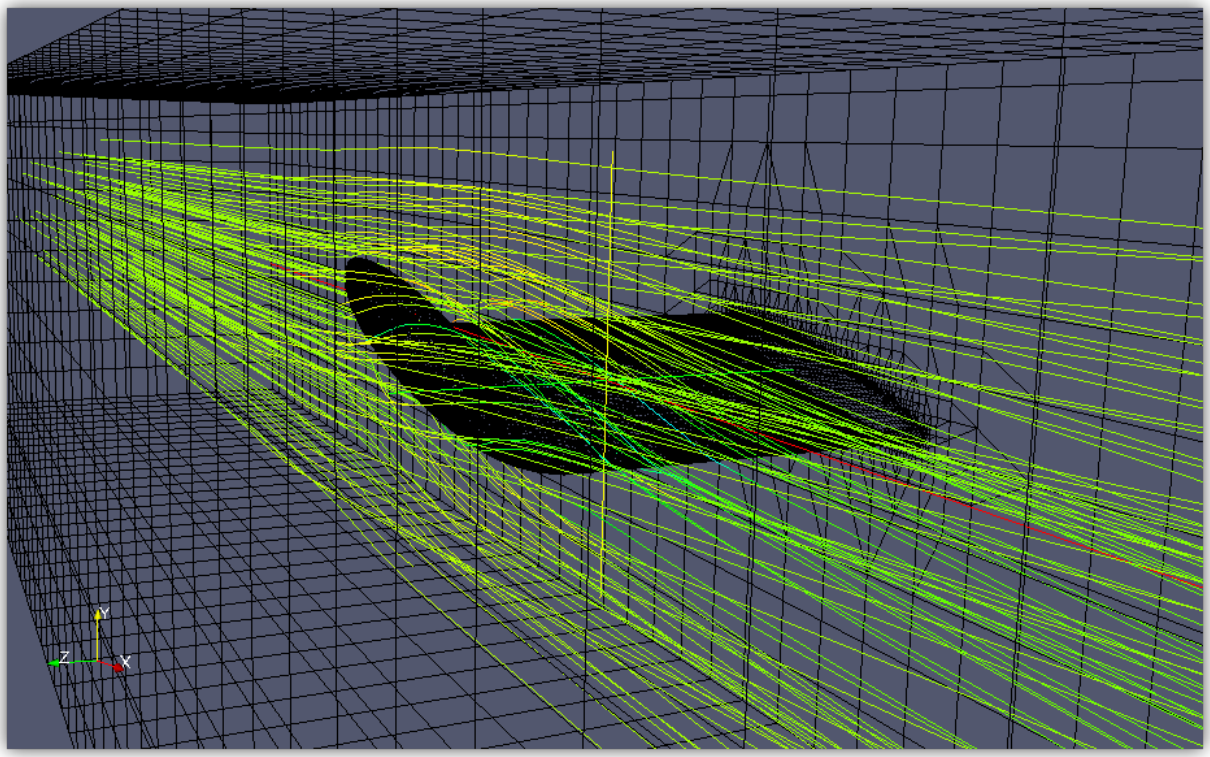

Inside the Computer-Generated High Speed Water Tunnel

Contents

1 Acknowledgments **1**

2 Abstract **2**

3 Project Motivation **3**

4 Premise of Wingtip Development for Hydrokinetic Turbine Application **4**
- 4.1 Cavitation . . . 4
- 4.2 Wingtip Vortices . . . 7
- 4.3 Hydrofoil Designs . . . 9
  - 4.3.1 EndCap . . . 9
  - 4.3.2 Simple Curve . . . 11
  - 4.3.3 The General . . . 12
  - 4.3.4 Das Boot . . . 13
  - 4.3.5 SplitTip . . . 14
  - 4.3.6 Design Choices . . . 15

5 Numerical Analysis **16**
- 5.1 Finite Element Analysis . . . 16
- 5.2 Open-Sourced Engineering . . . 20
- 5.3 Octave Generated 3-Dimensional .stl Geometry . . . 20
- 5.4 Computational Fluid Dynamics Analysis of Wingtip Devices . . . 22
- 5.5 Geometric Optimization Study . . . 24
- 5.6 Numerical HiCaT Simulations . . . 25
- 5.7 HiCaT Force-Balance Calibration . . . 26

6 Experimental Apparatus Design **28**
- 6.1 Base Foil Design . . . 28
- 6.2 O-Ring Groove Design . . . 30
- 6.3 Wingtip Manufacturing - Direct Metal Laser Sintering . . . 31
- 6.4 Tolerance and Machining Process . . . 31

7 Experimental Results and Discussion **34**
- 7.1 Pressure Profiles . . . 34
- 7.2 Lift and Drag . . . 38

8 Conclusion **40**
- 8.1 OpenFOAM - Future Development . . . 40
- 8.2 HiCaT Experiments - Future Development . . . 40

9 Bibliography **42**

10 Appendices **43**
- 10.1 Appendix A - OpenFOAM Images . . . 43
- 10.2 Appendix B - OpenFOAM Case Directory . . . 54
- 10.3 Appendix C - OpenFOAM User Guide . . . 55

List of Figures

1 Phase Diagram of H_2O. . . . 4
2 [Pressure Gradients over a Foil]Pressure Gradients over a Foil: (a)Normal Flow (b)Cavitating Flow. . . . 5
3 Wingtip Vortices . . . 7
4 [Plain Foil Cavitating Vortex]View of the Plain Foil cavitating wingtip vortex during experimentation. . . . 8
5 [Rendered views of Plain Foil]Various rendered views of Plain Foil. . . . 9
6 Alstom Turbine . . . 10
7 Rendered views of Simple Curve]Various rendered views of Simple Curve. . . . 11
8 [Rendered views of The General]Various rendered views of The General. . . . 12
9 Atlantis Resources Corporation tidal turbine deployment in Orkney [12]. . . . 12
10 Rendered views of Das Boot. . . . 13
11 Rendered views of SplitTip. . . . 14
12 Lift over drag of simulated foils . . . 15
13 Cross Sectional View of Hydrofoil . . . 16
14 FEA Mesh Convergence . . . 18
15 FEA Final-Mesh . . . 18
16 FEA von Mises Yield Stress . . . 19
17 FEA Deflection . . . 19
18 X,Y,Z Point Cloud Generation . . . 20
19 2-Dimensional Point Cloud Views . . . 21
20 3-Dimensional Point Cloud View . . . 22
21 Parallel Processing Case Directory Process . . . 23
22 SplitTip Sketch with Dimensions . . . 24
23 SplitTip Optimization . . . 25
24 Lift Calibration . . . 26
25 Drag Calibration . . . 27
26 Exploded View of Experimental Apparatus . . . 28
27 Isometric View of Final Wingtip Devices . . . 29
28 Soft Jaws . . . 33
29 Pressure Profile of the Endcap . . . 34
30 Pressure Profile of The General . . . 35
31 Pressure Profile of SplitTip . . . 36
32 Pressure Differential about Wingtip Devices . . . 37
33 Experimental vs. Computational Lift and Drag . . . 38
34 Lift over Drag Comparison . . . 39
35 CFD - Plain Foil View(1) . . . 43
36 CFD - Plain Foil View(2) . . . 44
37 CFD - The General View(1) . . . 45
38 CFD - The General View(2) . . . 46
39 CFD - SplitTip View(1) . . . 47
40 CFD - SplitTip View(2) . . . 48
41 CFD - SimpleCurv View(1) . . . 49
42 CFD - SimpleCurv View(2) . . . 50
43 V-Back Vorticity Slices . . . 51
44 ParaView - The General Pressure Profile . . . 51
45 ParaView - SplitTip Vorticity . . . 52

46 ParaView - SplitTip Pressure Profile 52
47 Blender - SplitTip Vorticity 53
48 V-Back Vorticity Magnitude Visualization 53
49 Case Directory 54

1 Acknowledgments

We would like to give a special thanks to the following project contributors, without which this project would not have been achievable:

- Project Advisers, Martin Wosnik and Ivaylo Nedyalkov
- Special Thanks to Joe Gabriel and Natalie Alford of Turbocam.
- Scott McCambell of the UNH Engineering Machine Shop
- Aaron Bolton and Phil Demaine of the UNH Space and Science Machine Shop
- The multitude of developers of *Linux, OpenFOAM, Meshlab, GNU Octave, ParaView, Blender,*and the communities that support them.

2 Abstract

The primary goal of this project was to create a numerical and experimental testbed for developing wingtip devices for marine applications, in particular Marine Hydrokinetic (MHK) turbines. The numerical studies were performed using *OpenFOAM*, a C++ toolbox. The numerical simulations provided profiles of pressure, velocity, and vorticity, as well as lift and drag values for each device.

From the simulation studies, novel devices coined the General and SplitTip were found to greatly reduce the effects of wingtip vortices, as compared to a generic wing.

The purpose of the experimental apparatus was to test various wingtip devices without creating full turbine blade sections for each device. The testing apparatus was designed such that four pressure measurements could be taken at various locations along the wingtip. Similarly these pressure-bores may be used to test the effects of injecting liquid water, or other mass, into the flow.

Achievements of this project provide an adequate means of simulating and testing hydrokinetic turbine tips. Computer based simulations exploited the benefits of computational fluid dynamics to accurately and rapidly develop complex devices at low cost. Real-world experiments performed in the HiCaT provided verification of CFD results. The numerical and experimental test-beds developed for the project will expedite future work on the design and testing of advanced hydrokinetic wingtip devices.

3 Project Motivation

MHK turbines are turning the tides as viable renewable energy conversion devices. MHK turbines operate under similar principles as wind turbines, however require strict design considerations due to various factors:

1. As with wind-turbines, wingtip vortices are a major contribution to drag on the turbine blades, thus increasing structural demands and reducing performance.
2. Pressure reductions over the turbine blades can promote cavitation (liquid water turning to vapor due to low pressures rather than high temperatures as with boiling). Cavitation also affects the lift and drag characteristics of blades. Furthermore, the shedding and collapse of vapor-pockets along the turbine-blade produce substantial forces; leading to blade oscillation and blade-material degradation.
3. Bio-fouling in marine environments is a concern for continuous, low-maintenance turbine operation.
4. Although operation occurs at lower speeds than wind turbines, water-turbines are able to produce substantial power due to the greater working fluid density. However, with the fluid density being 3 orders of magnitude greater than air, the stresses experienced by MHK turbines are similarly much greater.

The goal of this project was to develop a numerical and experimental test-bed for the design, development, and optimization of wingtip devices for MHK turbines. The goal of these devices is to reduce the adverse affects of tip vortice and enhance performance. This is achieved by increasing lift, decreasing drag, controlling or avoiding cavitation, accounting for bio-fouling, and sustaining the stresses experienced in marine applications. The design approach included numerical simulations and testing of physical models. A computer simulated water tunnel was developed using the open-source computational fluid dynamics (CFD) package, *OpenFOAM*. Specifications for the CFD model replicate the UNH High Speed Cavitation Tunnel (HiCaT). Prior to experiments, hand calculations and Finite Element Analysis (FEA) using *SolidWorks* software were used to ensure the experimental test bed and wingtip devices were capable of withstanding significant lift forces. Finally, physical HiCaT experiments were performed to obtain experimental results for validation of the numerical simulations.

4 Premise of Wingtip Development for Hydrokinetic Turbine Application

4.1 Cavitation

In order to develop hydrofoil-wingtip devices which act as cavitation inhibitors, it is important to understand how and where cavititation forms. Cavitation is defined as the formation of vapor cavities in a liquid upon being subjected to reduced pressures. This may be illustrated by examining the phase diagram of H_2O. If held at constant temperature and exposed to large enough pressure reductions, liquid water enters the vapor phase. High temperatures also can induce vapor formation; however in turbine hydrofoil applications the temperature of the system remains relatively constant and is considered negligible in our studies. Cavitation as described is therefore a form of boiling water as a result of pressure reduction rather than heat addition, where the physical and thermodynamic processes of vaporizing water are the same.

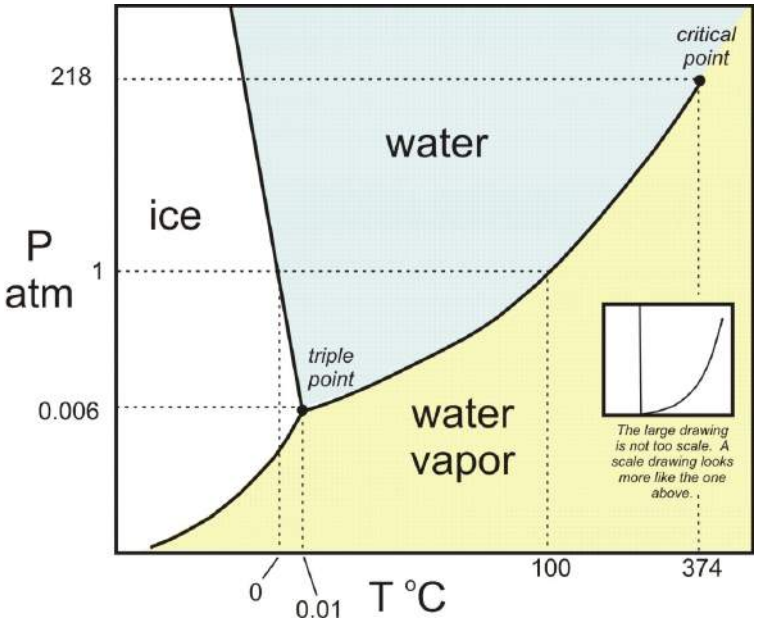

Figure 1: Phase Diagram of H_2O.

Pressure reductions in hydrodynamic flow exist mainly from disturbance in the flow equilibrium. For instance, if a fluid flow in a water tunnel test section experiences a velocity increase due to a reduction in cross-sectional area in the contraction section, the pressure at that point of the flow must also decrease; thus satisfying Bernoulli's equation, given as,

$$P_1 + \frac{1}{2} \cdot \rho \cdot V_1^2 + \rho g h_1 = P_2 + \frac{1}{2} \cdot \rho \cdot V_2^2 + \rho g h_2 \tag{1}$$

Therefore by analyzing the highest velocity or lowest pressure regions of flow over a hydrofoil surface, one may predict generally the areas which cavitation first occurs;

Hydrofoils in a moving liquid operate under the same principles as an Airfoil moving through air. As a hydrofoil is exposed to a fluid flow, areas of higher pressure will form on the side directly exposed to the flow while areas of lower pressure will form on the opposing side of the foil. From basic airfoil theory it may be inferred that cavitation will occur on the hydrofoil surface not directly exposed to the flow.

Cavitation will usually form first near the minimum pressure region, usually occurring at the leading edge. As the flow continues over the foil, within the low pressure region, the individual vapor pockets comprising the cavitating flow will continuously grow in size. Once the vapor pockets are exposed to higher-pressure regions downstream they begin to collapse.

Shedding vapor pockets create powerful, resultant forces which oscillate in high frequencies which have a number of negative effects on a machine. The collapsing vapor pockets damage most forms of metals and cause surface-material degradation. The forces can not only destroy a surface finish of a material, but may eventually cause significant pitting of the surface material. The frequency associated with cloud cavitation may also result in mechanical resonance; in which the regime forces on the foil fluctuates significantly with high frequency; on the order of 30 to 50 Hz). Mechanical resonance may result in increased stress amplitudes and catastrophic failure of a device. In Turbine applications cavitation must be mitigated or avoided to uphold the structural integrity and surface finish of the blades, which is both crucial to the normal, extended operation of a power-generating device.

Pressure profiles over a hydrofoil may be defined as force over area; as depicted below in Figure 2, [2].

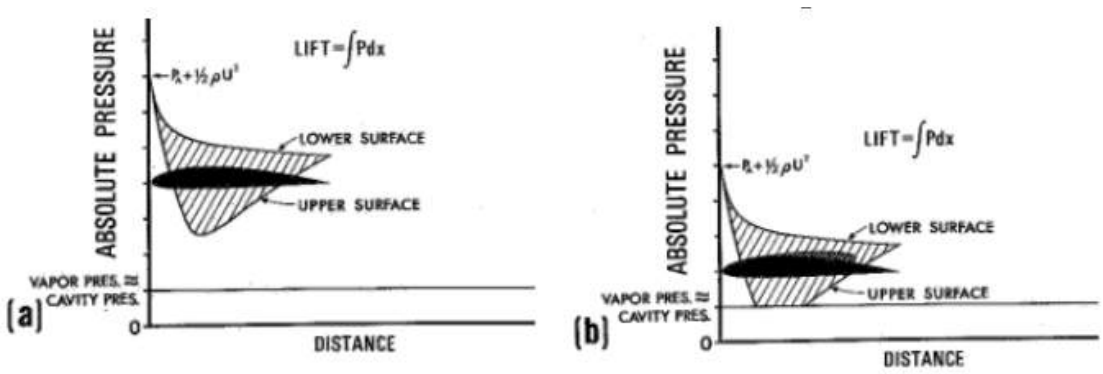

Figure 2: [Pressure Gradients over a Foil]Pressure Gradients over a Foil: (a)Normal Flow (b)Cavitating Flow.

By integrating the pressure regions over a given area the lift and drag forces may be determined. However, on any point of the hydrofoil the pressure region may not decrease beyond the cavity pressure, approximately the vapor pressure. Therefore as cavitation occurs, the physics of the flow changes, as well as the subsequent pressure distribution; as seen in Figure 2. In turn, in the presence of cavitating flow, the lift forces will decrease and drag forces will increase; also lift oscillations will occur as the attached cavities are periodically shed into the flow.

Cavitation in general may be described by the cavitation number, which quantifies cavitation and is given as,

$$\sigma = \frac{2 \cdot (P_\infty - P_c)}{\rho \cdot U_\infty^2} \tag{2}$$

Where P_∞ is the ambient pressure, P_c is the cavity pressure or vapor pressure, and U_∞ is the characteristic reference speed of the flow.

The cavitation number is the accepted means of scaling the degree of cavitation. It can be observed that the degree of cavitation occurrence becomes a function of flow velocity, ambient pressure, and vapor pressure. The cavitation number at which cavitation occurs is known as the cavitation inception number. At numbers above the cavitation inception number no cavitation occurs, while at numbers below the cavitation inception number, cavitation does occur.

As long as experiments are carried out at significantly large Reynolds numbers, Reynolds number dependence has a small effect. Cavitation model experiments may in turn be performed at lower speeds than actual operating speeds if the pressure is increased; or likewise by decreasing the pressure and keeping velocity constant.

4.2 Wingtip Vortices

Figure 3: Top left: CFD analysis on wind turbine showing wake effects behind the turbine including wingtip vortices [8]. Bottom left: Wingtip vortex forming around airplane wing [7]. Right: Photographer Christian Steiness: The above photograph shows the turbulence field behind the Horns Rev 1 offshore wind turbines. Unique meteorological conditions on 12 February 2008 at 1300 hours resulted in the wind turbines creating condensation (i.e. clouds of the very humid air), thus making it physically possible to see the turbulence pattern behind the wind turbines"[8].

Wingtip vortices are the major contributing factor to induced drag. They form at the tip of lift generating foils due to the pressure difference between the high and low pressure sides of the foil. The fluid from the high pressure region tends to move towards the low pressure side. Not only do wingtip vortices cause a significant amount of drag as well as loss of lift, but also contribute greatly to turbulence and energy loss of the flow. This is undesirable in arrays, as there is less energy available in the flow for turbines placed downstream. The image on the right of Figure 3 is a prime example of the effects of the wake effects of turbines of arrays. Wingtip devices have been shown to reduce the strength of wingtip vortices and decrease the induced drag on a foil.

At the center of a wintip vortex there is a low pressure zone. Inside the vortex the pressure can become low enough to cause cavitation of the fluid as shown in the image below from our experiment. This can be detrimental to machinery placed downstream if the cavitation bubbles collapse on it.

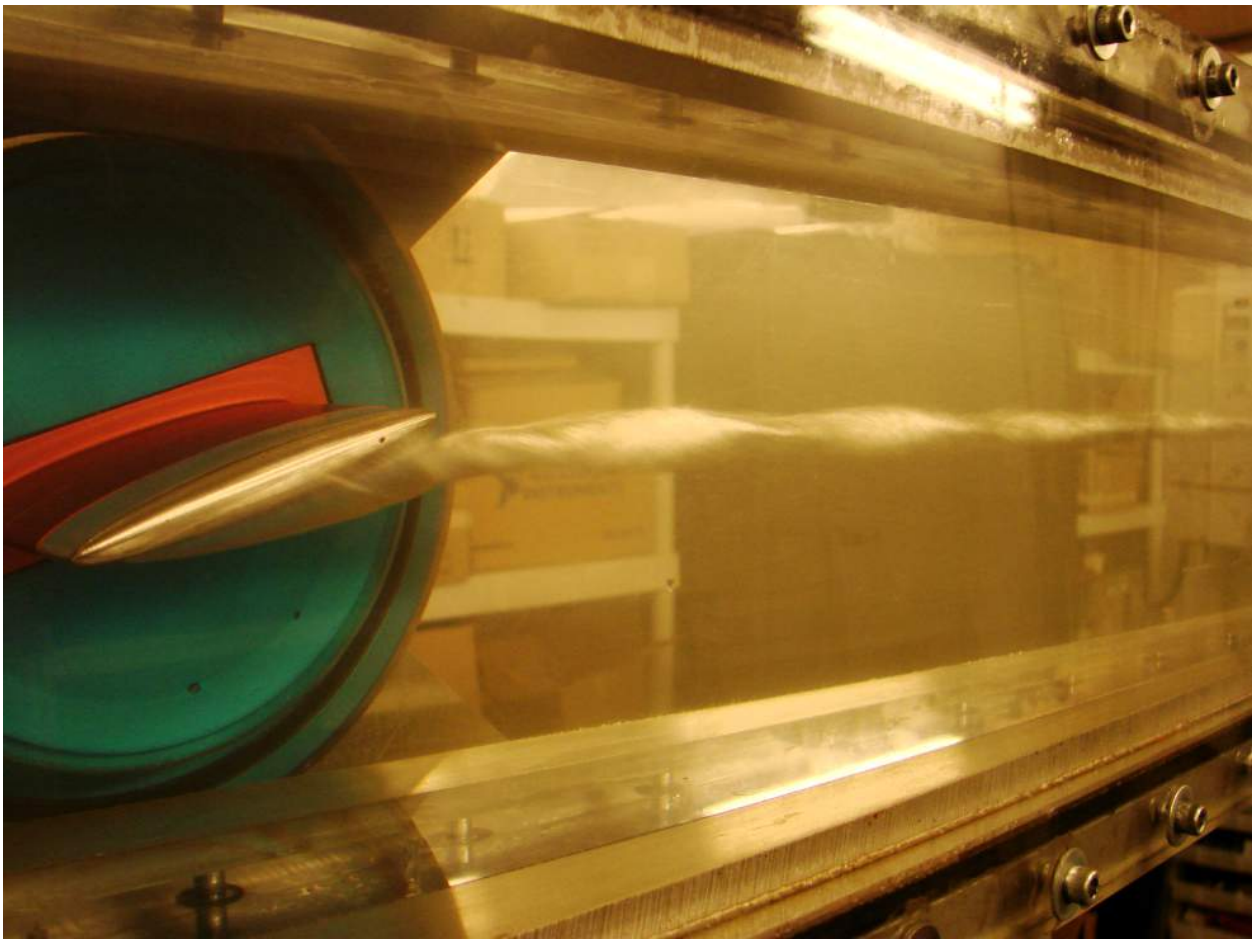

Figure 4: [Plain Foil Cavitating Vortex]View of the Plain Foil cavitating wingtip vortex during experimentation.

4.3 Hydrofoil Designs

The chord was maximized within set geometric configurations of the HiCaT force balance, in turn maximizing the measurable lift forces. The span was set to 3.25 inches, in turn centering the wingtip device in the center of the tunnel and decreasing the effects of wall-boundary conditions. The thickness of the foil was minimized to reduce the effects of blockage, without sacrificing the measurement capabilities of the apparatus; as discussed later in Base Foil Design.

4.3.1 EndCap

Figure 5: [Rendered views of Plain Foil]Various rendered views of Plain Foil.

Figure 6: Turbine of which the endcap is based[11].

The end cap was chosen as the reference wingtip device. It is consistent with the shape of the elliptical base foil section and ends in a revolved ellipse which rounds the end of the hydrofoil. The intent of this reference device was to model an existing device; similar to the tip used by Alstom, as seen in Figure 6.

4.3.2 Simple Curve

Figure 7: Rendered views of Simple Curve]Various rendered views of Simple Curve.

Simple Curve was a concept device that was meant to stop the flow from flipping from the high pressure side to the low pressure side. The main problem with this design was the large amount of blockage due particularly to the volume of the wingtip associated with its geometric configuration; a thinner device with cantered angles was in turn developed.

4.3.3 The General

Figure 8: [Rendered views of The General]Various rendered views of The General.

Figure 9: Atlantis Resources Corporation tidal turbine deployment in Orkney [12].

The General in its current form is in its 3rd iteration. It is loosely based off the tips shown in Figure 9.

4.3.4 Das Boot

Figure 10: Various rendered views of Das Boot.

This tip started off as a basic ellipse at the end. The from drag was found to be too high so this model was further developed. Form drag is still too high, it is recommended that the end profile be thinned out significantly why maintaining geometry.

4.3.5 SplitTip

Figure 11: Various rendered views of SplitTip.

The SplitTip device exploits phenomena of wingtip vortices in order to create counteracting vortices. When aligned correctly, the counteracting vortices have the potential to completely cancel one another out, reducing induced drag immensely. Some optimization of the device was undertaken and is described in Section 5.5. This device proved to perform well at 9 degrees angle of attack. There are many more variables to be studied within the geometry in order to make this a viable tip for real world application, but preliminary results show its potential is high.

4.3.6 Design Choices

The plot shown in Figure 12 shows lift over drag values for some of the foils considered for manufacture. A variety of tips were not shown as full data profiles were not taken. For example, V-back (shown in Figure 48 and Figure 43 as well as the elliptical wingtip (shown on the cover page) were eliminated as candidates after viewing results from 9 and 12 degrees angle of attack.

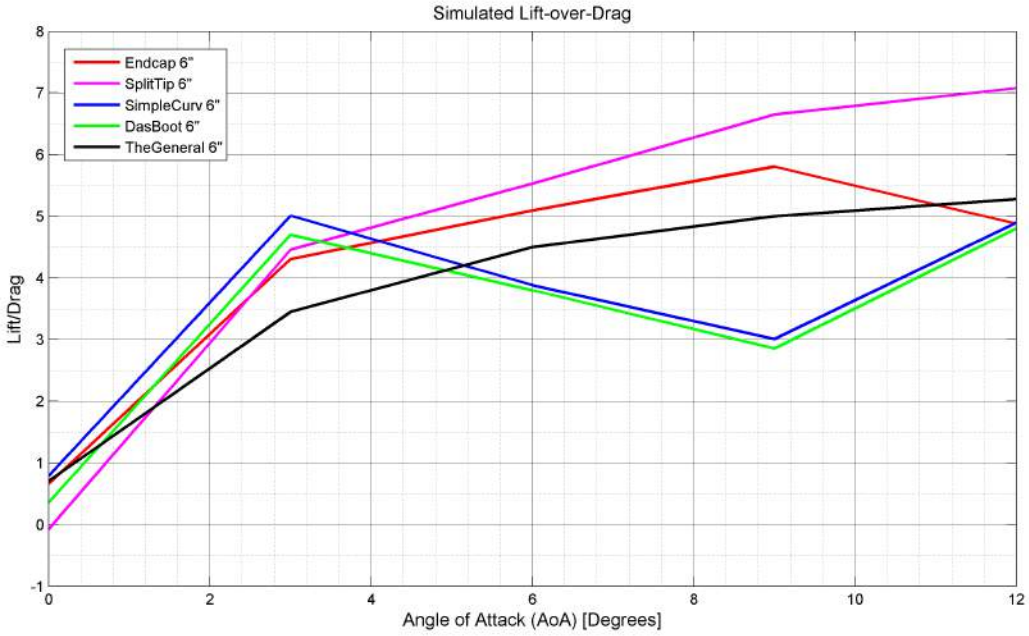

Figure 12: Lift over drag of simulated foils; this plot aided in the determination of manufactured tips.

As seen above, SplitTip and The General lift over drag results were better than those of Das Boot and Simple Curve. It appears that at 9 degrees angle of attack the wingtip vortices cause significant induced drag resulting in the low lift over drag number.

5 Numerical Analysis

5.1 Finite Element Analysis

As discussed, MHK turbines experience significant stresses given the high working fluid density. In order to design a hydrofoil which could withstand such stress it was necessary to perform aprior stress analysis on the experimental apparatus. The hydrofoil was initially modeled as a simply supported beam: Fixed on one end, with a single centralized force and hollow center. The forces acting on the hydrofoil were set to 400 lbf based on previous hydrofoil experiments performed in the HiCaT. Following hand calculations the hydrofoil was modeled with *SolidWorks* to confirm results through Finite Element Analysis (FEA).

Figure 13 shown below displays a cross sectional view of the hydrofoil, with the larger rectangular sketch representing the material cross sectional area and the latter representing the through-hole cross sectional area. The dimensions of the outer and inner rectangles were set such that the beam cross sectional area was equivalent to the hydrofoil cross sectional area, excluding through holes.

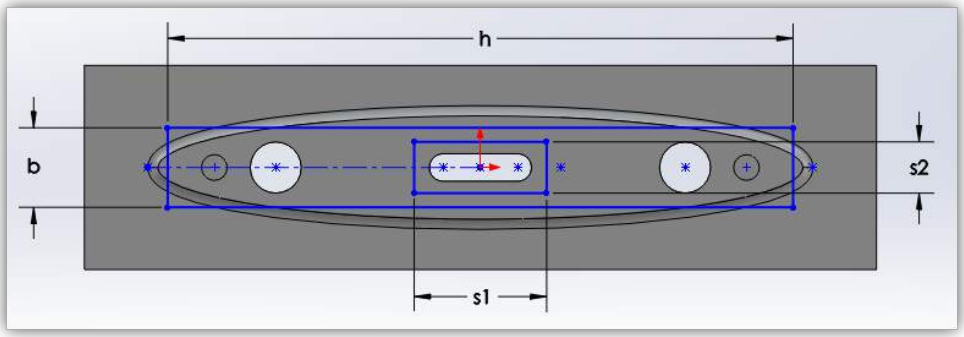

Figure 13: Cross Sectional View of Hydrofoil and Rectangular, Shape Estimates.

For a cantilever beam, end loaded, the maximum stress experienced at the fixed base of the beam is given as:

$$\sigma = \frac{P \cdot L}{Z}, \tag{3}$$

where P is the single, centralized force acting on the beam and L is the length from the location of force application to the fixed base of the beam.

Similarly the maximum deflection experienced at the free end of the beam is given as:

$$\Delta = \frac{P \cdot L^3}{3 \cdot E \cdot I}, \tag{4}$$

where E is youngs modulus of the material, I is the moment of inertia of the beam, and Z is the section modulus.

The section modulus may be defined as:

$$Z = \frac{2 \cdot I}{h}. \tag{5}$$

The moment of Inertia of a hollow, rectangular beam may be defined as:

$$I = \frac{bh^3 - (b - 2t)(h - 2t)^3}{12}, \tag{6}$$

where b is the height of the beam cross section, h is the width of the beam cross section, and t is the cross sectional area of the hydrofoil and beam material; where referencing Figure 13, t may be defined as:

$$t = (h \cdot b) - (s1 \cdot s2) = Area_{ellipse} \tag{7}$$

where the area of the ellipse may be defined by:

$$Area_{ellipse} = [\pi \cdot a1 \cdot b1] - 2 \cdot [\frac{\pi}{4} \cdot D^2] - [\pi \cdot r^2 + 2r \cdot l] \tag{8}$$

where $a1$ and $b1$ are the major and minor radius of the elliptical profile respectively, D is the diameter of the through hole, and r & l are the radius and length of the through-slot respectively.

Equation 8 was then iterated until the height and width of the cross sectional beam produced an area equal to the elliptical hydrofoil profile.

Assuming:

- Distance from Force to Fixed End, $L = (3.25/2)\ in = 0.041275\ m$
- Force, $L = 400\ lbf = 1{,}780\ N$
- Cross Sectional Area of Material, $t = 6.8595e - 04\ m^2]$
- Width of Beam Cross Section, $[h = 0.0804\ m]$
- Height of Beam Cross Section, $[b = 0.0100\ m]$
- Young's Modulus, $[E = 72\ GPa]$

Equation 3, and Equation 4 were used to respectively to solve for maximum stress, $\sigma = 239.3\ Mpa$ and maximum deflection, $\delta = 4.69e - 05\ m = 0.0018\ in$.

In order to perform FEA using *SolidWorks* software it was necessary to perform a mesh convergence. Mesh convergence is the process of increasing the mesh quality and parameters until the criteria of the study begin to converge. Figure 14 shown below displays the mesh convergence plot for the hydrofoil study.

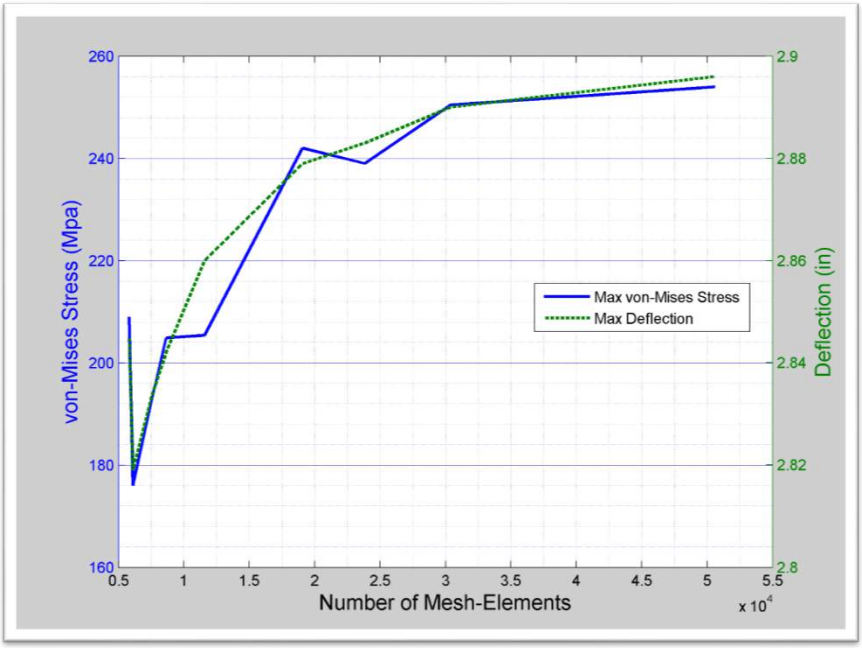

Figure 14: Mesh Convergence of *SolidWorks* Finite Element Analysis.

As seen from the above figure, the results began to converge as the number of mesh-elements approached 30,000; subsequently the mesh quality was set to 30,000 mesh-elements with a max element size of 0.12in. Figure 15 shown below displays the final mesh quality.

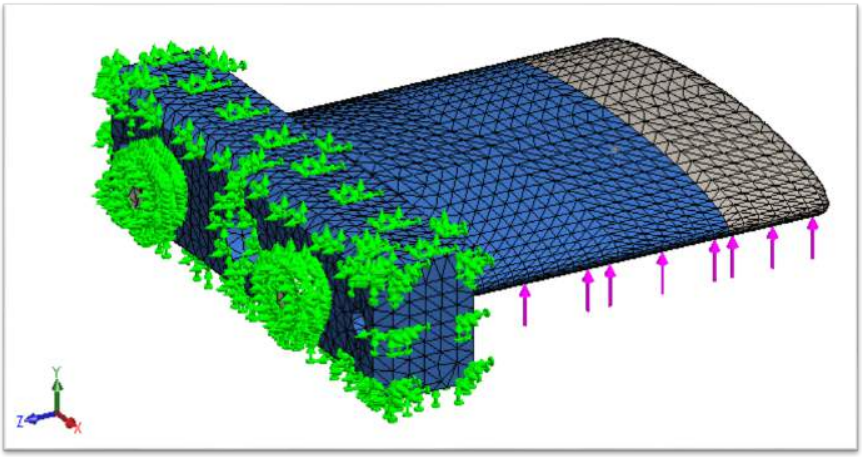

Figure 15: Isometric Veiw of Final FEA Mesh.

As seen in the above figure, the green arrows represent the fixed faces in the FEA study and the pink arrows represent the distributed load of $400lbf$.

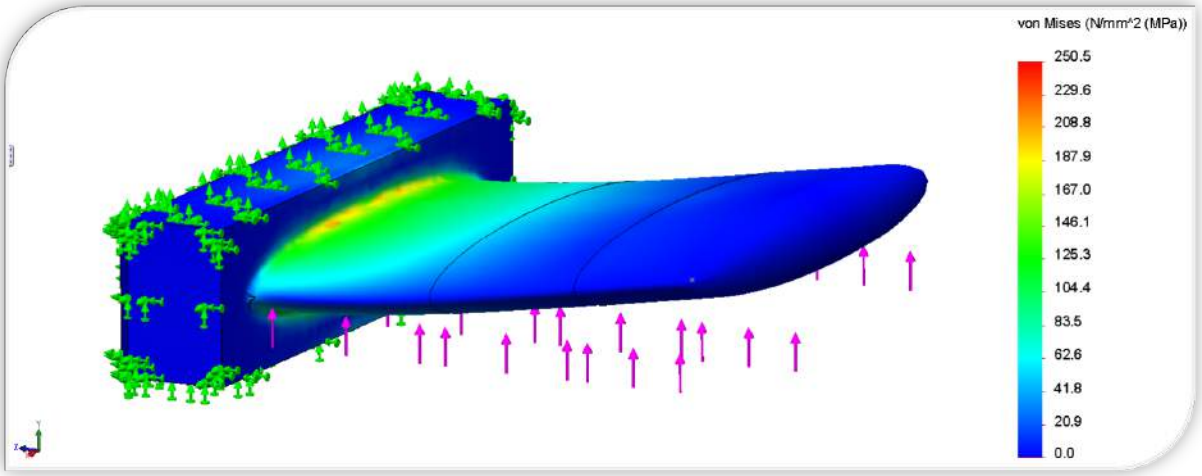

Figure 16: von Mises Yield Stress (MPa); as calculated by the FEA study.

As seen above in Figure 16, the maximum yield stress calculated by the FEA study was determined to be $\sigma = 250.5 Mpa$. Compared with hand calculations there exists only a 4.5% error.

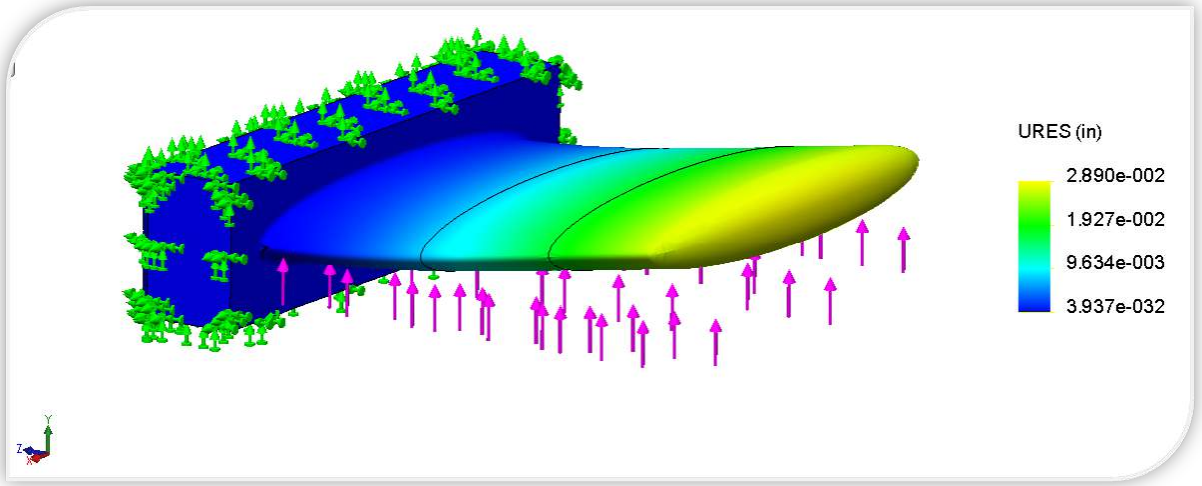

Figure 17: Hydrofoil Deflection (inches); as calculated by the FEA study.

As seen above in Figure 17, the maximum deflection calculated by the FEA study was determined to be $\Delta = 0.018 in$. Compared with hand calculations there exists a large amount of error: Based upon the accuracy of the maximum-stress hand calculations, and the accepted solutions for cantilever-fixed end beam, it is likely that $SolidWorks$ overestimated the deflection of the hydrofoil.

Based upon the results of the FEA study and hand calculations it was determined that Aluminum 7075-T6 would be the material choice for the base and extension of the Ex-

perimental Apparatus. Aluminum 7075-T6, with a yield strength of $500MPa$, provides a factor of safety of 2 under the maximum HiCaT-hydrofoil loading conditions. Aluminum 7075-T6 is also capable of being hard anodized which will aid in corrosion resistance and in preventing potential material-surface degradation caused by collapsing vapor pockets during cavitating flows. Aluminum 7075 T6 is also easily machinable, thus aiding in lowering the overall production costs of the apparatus.

5.2 Open-Sourced Engineering

This project posed a major difficulty in terms of funding. Commercial CFD packages are expensive and would have left us with limited funding remaining to manufacture the testing apparatus and wingtip devices. We decided to use *OpenFOAM* in order to avoid the cost of a CFD package. In *OpenFOAM*, we were able to develop a steady state simulation of the HiCaT. Using this simulation a variety of "existing" and novel wingtip devices were analyzed and some of the best resulting tips are presented. *GNU Octave* was used as a replacement for *Matlab* for meshing the SplitTip as well as creating automated optimization studies. *Meshlab*, *ParaView* and *Blender* were used as pre and post-processing tools respectively; allowing for the 3-D outputs to be rendered and analyzed.

5.3 Octave Generated 3-Dimensional .stl Geometry

Octave is a high-level programming language that is mostly compatible with *Matlab*. Generating geometry in this language was not trivial but is key to the development of automated optimization studies. Testing individual geometric variable becomes very simple using loops once a code is made to generate .stl outputs.

A series of curves were defined in the XY and XZ planes which described the center point of each ellipse as well as its chord length. Some number of points N are plotted around an ellipse defined in the function *ellipse.m* [6]. Ellipses are then rotated in the ZY plane so that each ellipse is tangent to the spline that defines its center. At this point the 3-D point cloud is ready to be rotated to the desired angle of attack using *rodrigues_rot.m* [5].

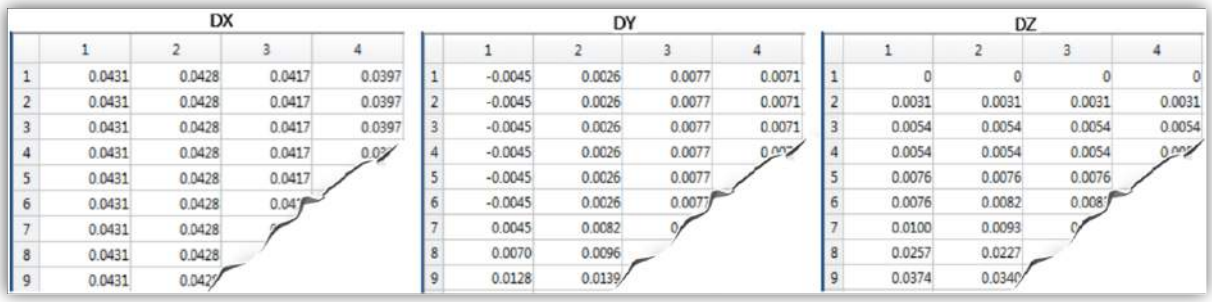

DX

	1	2	3	4
1	0.0431	0.0428	0.0417	0.0397
2	0.0431	0.0428	0.0417	0.0397
3	0.0431	0.0428	0.0417	0.0397
4	0.0431	0.0428	0.0417	0.03
5	0.0431	0.0428	0.0417	
6	0.0431	0.0428	0.04	
7	0.0431	0.0428		
8	0.0431	0.0428		
9	0.0431	0.042		

DY

	1	2	3	4
1	-0.0045	0.0026	0.0077	0.0071
2	-0.0045	0.0026	0.0077	0.0071
3	-0.0045	0.0026	0.0077	0.0071
4	-0.0045	0.0026	0.0077	0.00
5	-0.0045	0.0026	0.0077	
6	-0.0045	0.0026	0.007	
7	0.0045	0.0082	0	
8	0.0070	0.0096		
9	0.0128	0.0139		

DZ

	1	2	3	4
1	0	0	0	0
2	0.0031	0.0031	0.0031	0.0031
3	0.0054	0.0054	0.0054	0.0054
4	0.0054	0.0054	0.0054	0.00
5	0.0076	0.0076	0.0076	
6	0.0076	0.0082	0.008	
7	0.0100	0.0093	0	
8	0.0257	0.0227		
9	0.0374	0.0340		

Figure 18: Dimensional Changes in the X, Y, and Z axis for point cloud generation.

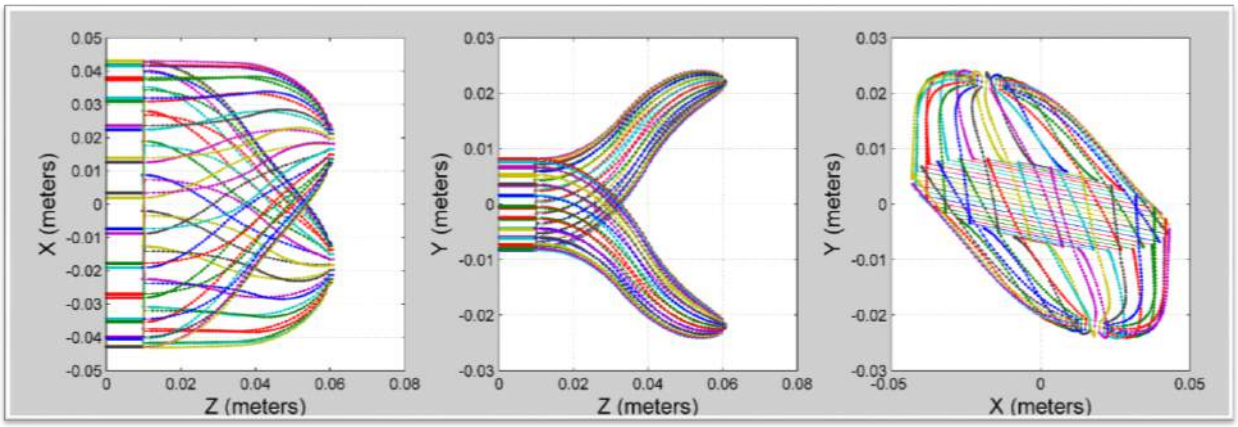

Figure 19: Visualization of the point cloud in 2 dimensions.

With the desired 3-D point cloud geometry generated shown in Figure 19 and Figure 20, a script that would convert from point cloud to stl was needed. Existing point cloud to stl algorithms did not work for the geometry created. *Meshlab* and *Blender* also had trouble meshing the point cloud. It was decided to write a matlab script using standard stl notation shown below:

```
facet normal ni nj nk
    outer loop
        vertex v1x v1y v1z
        vertex v2x v2y v2z
        vertex v3x v3y v3z
    indent endloop
endfacet
```

Starting with the first ellipse generated, the first two points on the ellipse were called. The first two points from the next ellipse were also called. This created a rectangle which was broken into two triangles. Normals were calculated and all data were written to the Foil.stl file.

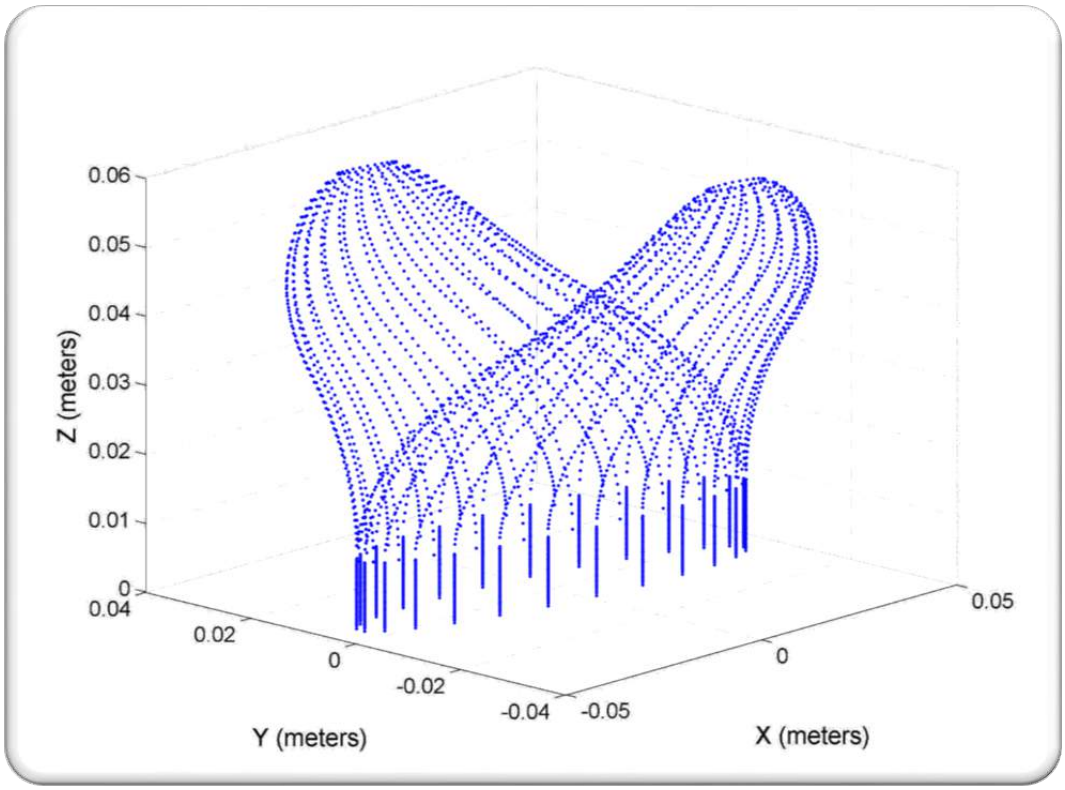

Figure 20: Visualization of the 3-D point cloud.

5.4 Computational Fluid Dynamics Analysis of Wingtip Devices

One of the primary goals of this project was to create a simulation of the HiCaT tunnel that could be compared to test results. This simulation case directory will serve as a starting point for future projects so that it's accuracy can be continually improved. Using simulations in advance of creating models is also good practice, saving time and money as well as allowing for complex and unorthodox devices to be tested without the fear of failure associated with pricy devices. The simulation would allow the modelling of many potential devices and help in making design decisions for the printed tips.

To create this legacy simulation bed, the open source computation fluid dynamics package *OpenFOAM* was used. *OpenFOAM* is a C++ toolbox with that allows user to edit a series of text files in order to set all the parameters necessary to create a CFD test. The uses of this program are widely varied from wind tunnels and wave tanks to casting simulations. After significant research and much trial and error a stable version of the HiCaT was generated.

A multitude of problems were encountered along the way. *OpenFOAM* has a steep learning curve. There are a few tutorials available but none related directly to the HiCaT. After running through many of the tutorials and learning the ins and outs of wind tunnel simulation, it was decided to base the HiCaT model off of a wind tunnel case directory and change the necessary criteria from there. This was essentially pointless since after all was said and done almost every variable was changed as well as all of the computational models. Creating a well correlated mesh for each wingtip was the next problem. The function *snappyHexMesh* is used to combine *STL* files with the tunnel mesh

which is created using the function *blockMesh*. The results of *snappyHexMesh* showed many spikes on the surface of the wingtips that affected the simulation and caused significant drag. Solving this took far too much time and was never quite perfect. Fortunately an update to *OpenFOAM* came out in February along with a new version of *snappyHexMesh* that did not have any of the problems previously experienced.

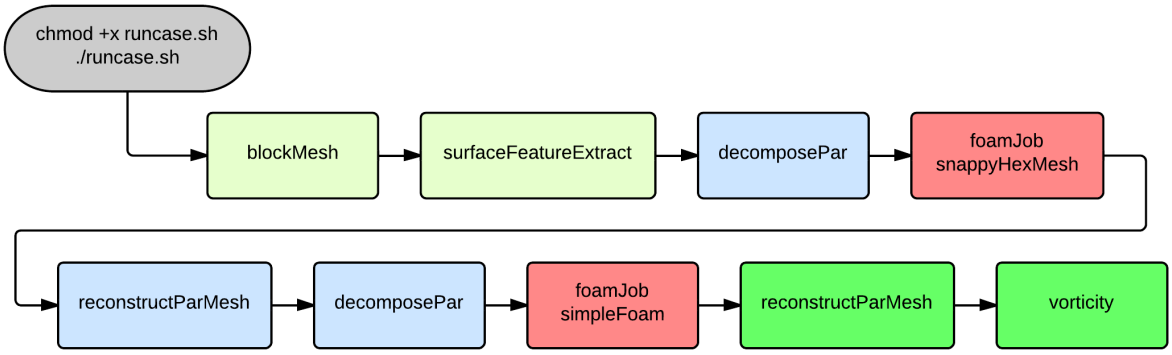

Figure 21: Process followed to run one case directory using parallel processing.

The stable version case directory was duplicated and each designed foil at angles of attack from 0 to 12 in 3 degree increments. A new stl file was created for each test and placed in the triSurface folder. From this folder the features of the file are analyzed using a built in function *surfaceFeatureExtract*. The resulting *eMesh* file, the stl, and the unrefined mesh are called on by *snappyHexMesh*. This function runs in parallel using *foamJob -parallel* to distribute the work on multiple processors. This function combines the stl and unrefined mesh to create a series of meshes (8 for my computer). *reconstructParMesh* is called on to put the separate meshes back together so that they can once again be broken apart by *decomposeParMesh*. Once decomposed, *foamJob* is called on again, but this time it is used to run *simpleFoam*. *simpleFoam* is a steady state solver that allows the user to see any number of variables called on in the case directory. Pressure, velocity, and vorticity profiles are all created during this process.

5.5 Geometric Optimization Study

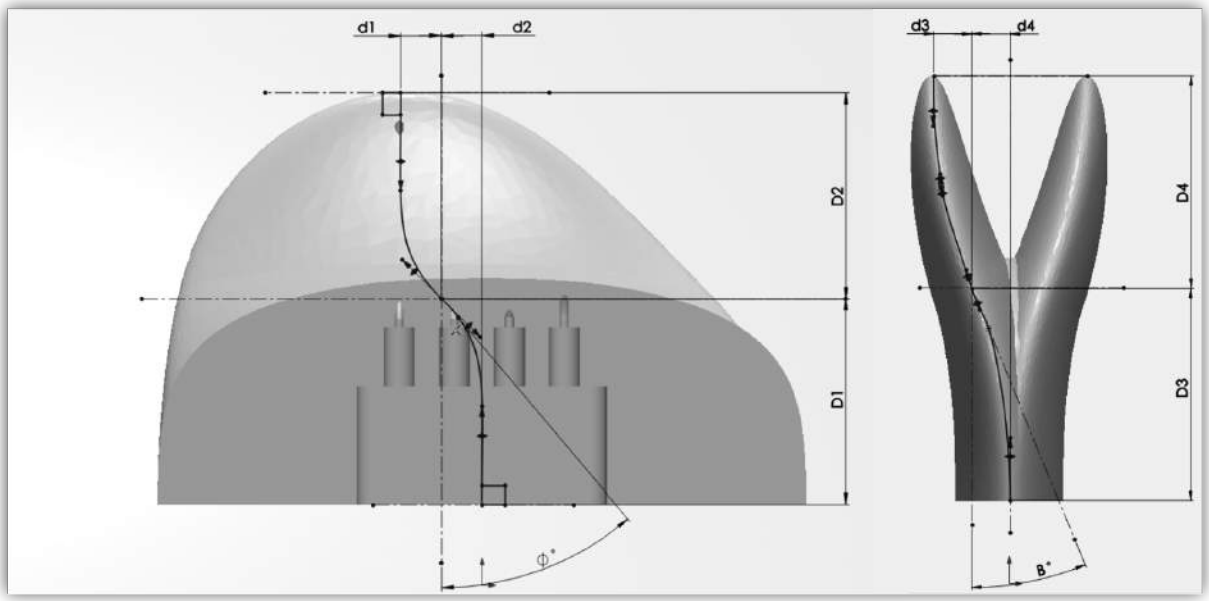

Figure 22: Sketch of SplitTip dimensional parameters, with Beta being the mid-wing angle.

Since the SplitTip was only a conceptual device, there was no consensus on which parameters were meaningful and what values would be reasonable to set them as. *GNU Octave* was used to write a script that copied an empty case directory of the HiCaT (although a larger 6" foil was used and the tunnel was set to 0.4 m x 0.4 m to eliminate the effects of the walls and to make sure the foil was generating enough lift for the tip to act correctly). The flow for these tests were set to 8 m/s (what we originally thought we would be testing at in the HiCaT) and run from 0-12 degrees angle of attack. The FIGURE ABOVE shows the SplitTip and the geometric variable optimized, called the mid wing angle. Results from OpenFOAM (shown in Figure 23) led to the use of $\pi/4$ as the chosen mid wing angle.

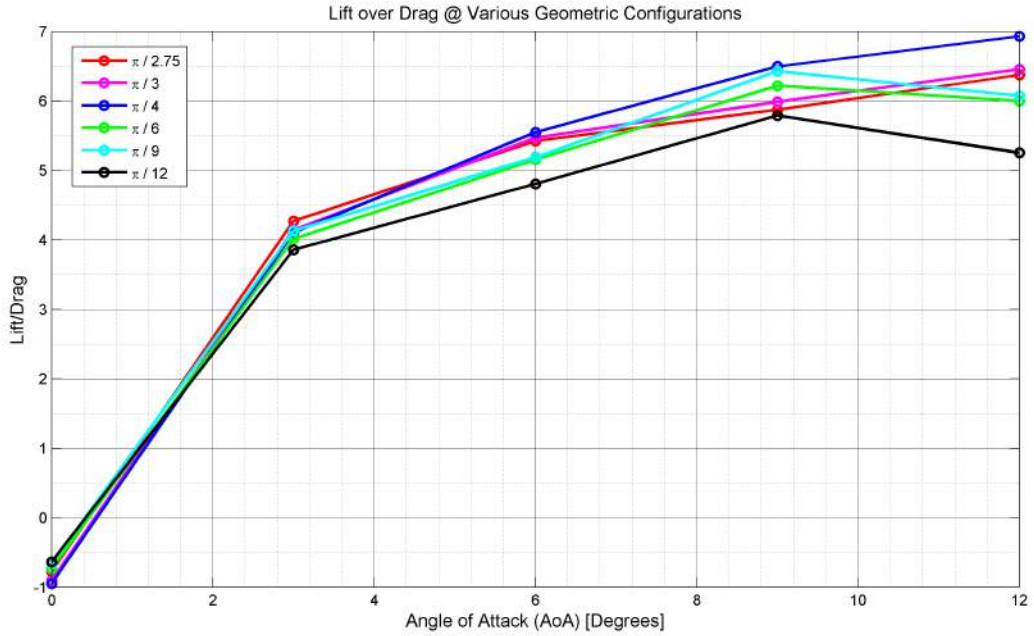

Figure 23: Mid wing angle optimization of the split tip.

5.6 Numerical HiCaT Simulations

The criteria used in each directory are set duplicate the dimensions of the HiCaT (6" x 6" cross section) and the conditions expected during testing: 100 kPa atmospheric pressure (ambient was 101.28 kPa for Plain Foil experimental testing and 102.6 for The General and SplitTip) and 4 m/s flow speed. One key criteria for future development is to input a velocity profile at the inlet of the HiCaT simulation as this was set to be uniform with some turbulent kinetic energy (0.24 J).

5.7 HiCaT Force-Balance Calibration

CFD right hither

The force balance on the HiCaT is an Ocean Engineering senior design project from 2012. Using 8 strain gages adhered the balance simultaneously measures the lift and drag on any foil in the tunnel by measuring the strain on 2 sets of plates.

Like any instrument, the force balance on the HiCaT must be calibrated before it can be used to find the relationship between the change in strain gage resistance and lift and drag. The calibration procedure for the HiCaTs force balance consists of hanging sets of weights off a calibration foil and reading the changes in voltages to determine the drag calibration curve. To calibrate the balance for drag a pulley is used to change the direction of the force applied to the balance in the drag direction.

Example calibration curves for lift and drag are included below as Figure 24 and Figure 25 respectively.

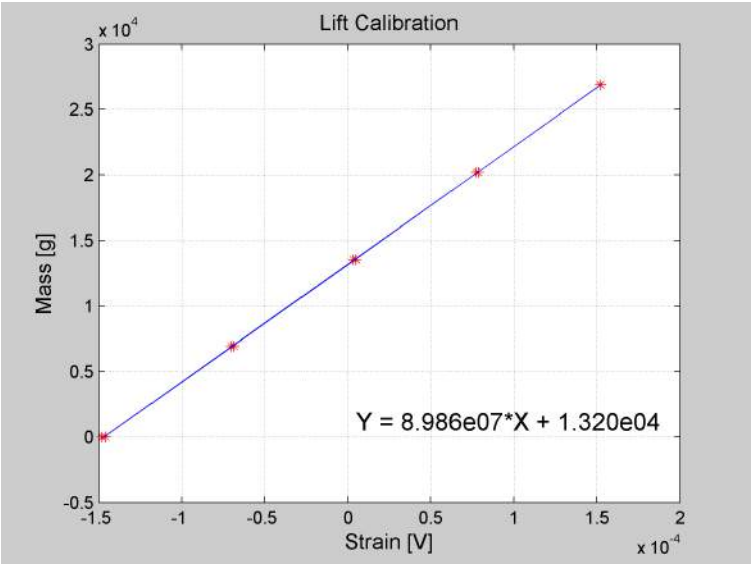

Figure 24: Lift Calibration Data & Line of Best Fit.

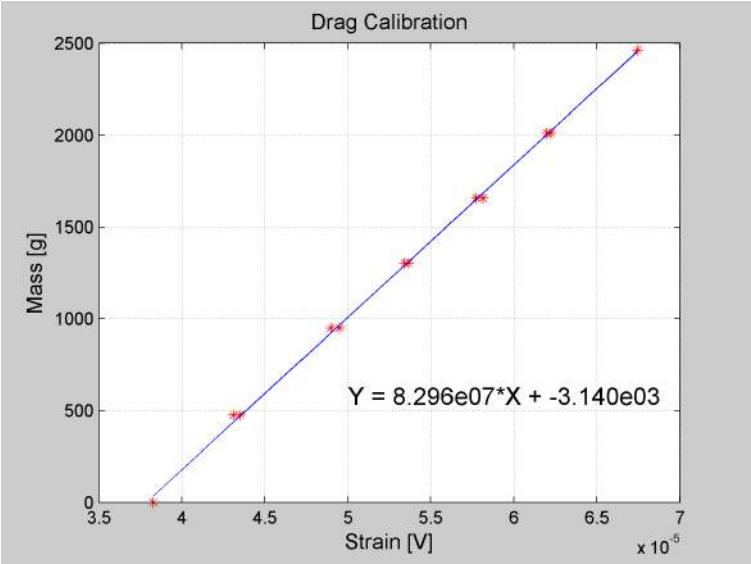

Figure 25: Drag Calibration Data & Line of Best Fit.

Our calibrations yielded sensitivities of 8.99*107$\frac{g}{V}$ for lift and 8.30*107$\frac{g}{V}$ for drag. The offset voltages were determined directly from measurements obtained at zero flow speeds with the hydrofoils mounted in place.

Although the force balance does consistently measure small amounts of lift and drag, its design is not flawless and not all measurements with it are accurate. Difficulties have arisen with calibrating the drage force by use of a rope and pulley. The pulley does have slight amounts of friction, which can contribute to hysteresis in the calibration of drag. Currently a nylon clothesline rope is used to calibrate the force balance. This rope tends to strain. If the rope is not lifted off the pulley between each weight interval on the down calibration the strain in the rope from the previous interval will remain in the rope and that force will remain on the balance leading to an increase in hysteresis. It was also observed that even slight movements of the electrical connectors that relay the signal from the strain gages to the NI DAQ unit had an effect on the measured strain. This is most likely due to small changes in contact resistance in the connectors. It was also determined that the force balance will loose calibration after cavitating flows. It is not known why this phenomena occurs, so our experiments attempted to avoid cavitation during the lift and drag measurement tests. There also seems to be a dependence on pressure for readings of lift and drag. This may be due to the displacement of the latex seal on the force balance beam creating reaction force on the beam of the balance. If the seal is allowed to move than this reaction force will create variable amounts of moment on the beam.

The design of the force balance could be improved to increase its utility and ergonomics. Currently the method for setting and changing angle of attack is cumbersome. Two screws are used to hold the angle of attack should be replaced with a quick release device capable of maintaining the angle of attack during operation. Also protractor could be installed to set the angle of attack, instead of the current digital hand-held device. Longer cables could also be purchased to link the force balance to the NI DAQ unit with more mobility around the water tunnel during testing; in turn preventing any interference of cable disturbance.

6 Experimental Apparatus Design

6.1 Base Foil Design

Design considerations of the experimental apparatus included interchangeable wingtips, varying wingtip sizes, precision alignment, appropriate material choice, and experimental measurement capability. The final exploded assembly of the reference base foil may be observed below in Figure 26

Figure 26: Exploded View of Experimental Apparatus. Left to Right: Base, Extension, EndCap (or other wingtip device).

As seen in the above figure, the apparatus was designed such that multiple wingtip devices could be tested on the same platform; thus reducing production time & cost. The overall length of the hydrofoil assembly, excluding the rectangular mounting block, was set to 3.25". This dimension allowed the mid-tip of the hydrofoil to be centered in the 6" HiCaT test-section; minimizing the wall-boundary effects on the wingtip vortices.

With consideration to variable wingtip designs and dimensions, an extension was added to the assembly to allow for possible, future wingtips of varying lengths. To ensure precision alignment between the base, extension, and wingtip devices, 2 hardened stainless steel dowel pins were added between each mating surface. Finally a slotted through cut and O-ring groove were added to the apparatus to allow for experimental measurement and operations; such as pressure readings or mass injection.

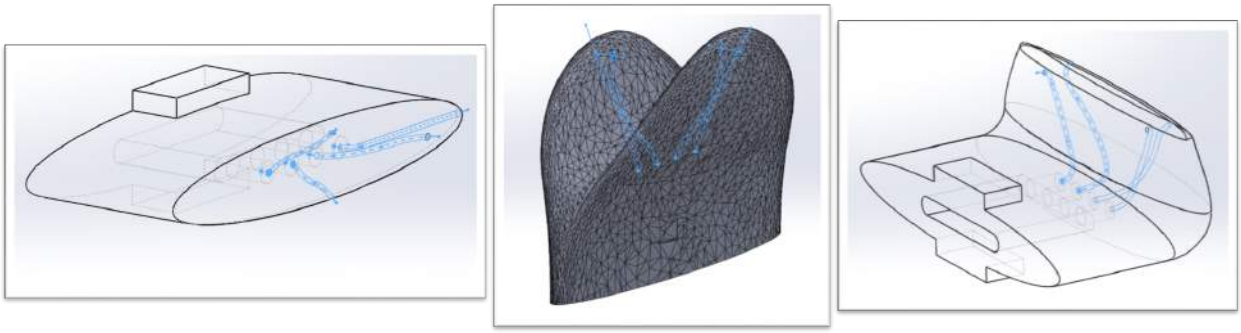

Figure 27: Isometric View of Final Wingtip Devices and Internal Pressure/Injection Bores. Left to Right: Reference EndCap — SplitTip Device — General Device.

As seen above in Figure 27, each device was equipped with four internal bores, each connected to flexible EVA tubing by a barbed hose fitting. The geometry of the existing force balance limited the number of measurement tubes to four tubes of 0.125" outside diameter. For each foil it was determined that most beneficial form of measurement would be pressure readings across the high and low pressure sides of a given wingtip device; as this is directly related to wingtip vortex strength. For the endcap it was determined that the average pressure change would be measured at the center of the foil, and the remaining two pressure bores would be placed near the trailing edge of the foil; thus allowing for direct mass injection into a cavitating vortex.

6.2 O-Ring Groove Design

O-Ring groove design must consider both sealing and material stress design per the dynamic or static application. For the case of the mating elliptical faces of the experimental apparatus it was necessary to design for proper sealing in a static situation under high water pressures. Also given the thin walled features between the O-ring groove and outermost edge of elliptical profile, it was necessary to ensure the the shear stress on the grooves did not exceed the yield of the material; refer to Figure 26.

The amount of sealing achieved by an O-ring is given as:

$$squeeze = 100\frac{w-c}{w}, \tag{9}$$

where w and c are the O-ring width and groove depth respectively.

The ratio of cross sectional areas of the O-ring and groove is defined as:

$$AR = \frac{A_o}{A_g}, \tag{10}$$

where A_o is the O-ring cross sectional area:

$$A_o = \pi \cdot w^2/4 \tag{11}$$

and A_g is the groove cross sectional area:

$$A_g = c \cdot g, \tag{12}$$

where g is the groove width.

Finally the shear stress on the groove may be defined as:

$$\sigma_g = p_g \cdot c/w_g, \tag{13}$$

where p_g is the pressure acting on the groove, c is the depth of the groove, and w_g is the distance from the groove to the nearest edge.

The design of the apparatus O-ring groove assumed static sealing in vacuum. For this application it is recommended to design for a higher squeeze value then the general 15-20%. The sealing quality of the O-ring is increased significantly at a squeeze of 30%, where the effects of further increasing squeeze to 50% shows negligible changes. Under these considerations, equation 9 was rearranged to solve for desired groove depth, c; where the width of the O-ring w, was set to 0.07" due to geometric constraints of the apparatus, and the squeeze was set to 30% [4].

To ensure proper sealing it is also necessary to keep the ratio of cross-sectional areas AR, less than 100%. By setting AR to 85%, equation 10 was rearranged to solve for the subsequent O-ring groove width g.

Given the dimensions and squeeze of the O-ring groove, the resultant stress of the sealing application could be analyzed to ensure it would not exceed that of the material yield strength. The pressure acting on the groove is dominated by the resulting pressure from squeezing the O-ring, which may reach values of 100 pounds per square inch of seal [4]. Using equation 13, and given the minimum wall thickness of 0.0421" between O-ring groove and outer face, the shear stress was determined to be $\sigma_g = 283psi$; more then three orders of magnitude less than the yield of Aluminum 7075 T6.

6.3 Wingtip Manufacturing - Direct Metal Laser Sintering

Given the complex geometries of our developed wingtip devices it was determined that conventional CNC operations were too time-consuming and costly. With this we began to research more unconventional methods of prototype production, and learned of Direct Metal Laser Sintering (DMLS). DMLS is a metal fabrication technology which fuses metal powder into a solid part by melting the powder through high powered laser exposure. The machine operates on the principles of the 3-dimensional rapid prototyping; in which a given part is broken down into many layers and sintered in these subsequent layered steps.

Working with Turbocam of Dover, NH; DMLS was chosen as the best production method for our wingtip devices for the following reasons:

- Capable of printing off of 3D-CAD models.
- Option of Super-Alloys [Stainless Steel PH1] or [Nickel Alloy Inconel-718].
- Precision printing [0.787e-03 to 1.57e-03] inch layers.
- Machine tolerances of 0.002".
- Minimal achievable wall thickness of 0.012".

6.4 Tolerance and Machining Process

Alignment of the assembled base foil sections will be achieved using hardene, 0.125" stainless steel dowel pins; located on each mating face of the assembly. The pins should be permanently seated in one section of foil and be removable from the other. This will allow the foil sections to be accurately interchangeable, and more importantly provide geometric repeatability throughout multiple experiments.

The permanent side of the pin was in turn designed as a press fit mate; in which a press fit mate requires a 0.0001" $\rightarrow$ 0.0003" interference. To achieve pin removability without sacrificing dimensional precision, the removable section of the pin was designed to be a tight, slip-fit mate; in which a tight, slip-fit mate requires a 0.0003" $\rightarrow$ 0.0006" clearance.

Given the material selection of Aluminum 7075 T6, it was determined that hard anodizing would be necessary to prevent surface fatigue; primarily in experiments where cavitation is present. The anodizing thickness was set to 0.001", in which 50% of the substrate penetrates the material and 50% of the substrate is deposited on the surface. With this consideration it was determined that an additional 0.0005" would be added to the outer surface of the DMLS, 3D-CAD models.

A sample DMLS part was received by Turbocam in order to determine necessary polishing methods and subsequent surface material losses due to these polishing techniques. The elliptical sample was first measured both at the major and minor ellipse diameter before polishing. A series of polishing steps were performed on the part to achieve a smooth surface finish, including: (1_{st})Bead Blasting, (2_{nd})Rough Filing, (3_{rd})100 Grit Sanding, (4_{th})400 Grit Sanding, and (5_{th}) Buffing-Wheel Polish. Post polishing, measurements again were taken at the same locations, from which it was determined the necessary polish techniques removed just under 0.002". With this consideration it was determined that an additional 0.002" would be added to the outer surface of the DMLS, 3D-CAD models.

Given the achievable, dimensional accuracy of Turbocam's DMLS machine, it was determined that the final machine processes would be completed by conventional CNC operations at the University of New Hampshire, Engineering machine-shop. These final CNC operations consisted of:

- Milling the mating face of the wingtip device.
- Drilling & Tapping two $1/4" - 20$ screw holes.
- Drilling & Reaming two 0.125" Press Fit bores.

Although the final machine processes themselves are relatively simple, the complex geometry and material selection require additional considerations.

First: Nickel Alloy Inconel-718 is an extremely hard material which work hardens very quickly due to its high nickel content, lending to rapid thermal gains and high temperatures during machine machine processes. In order to prevent excessive tool wear and possible failure, a series of cooling devices were set up on the CNC machine. The first device supplied a steady stream of non-toxic cooling liquid while the second device provided a constant supply of ice-cold air though a patented compressed air vortex cooler.

Second: The elliptical geometry of the wingtip devices does not allow for sufficient clamping friction between the CNC vice jaws. Given the high stregth of Inconel it is necessary to ensure adequate clamping power of the part aprior to any machine processes. Working with the University of New Hampshire Space & Science machine-shop, a set of custom soft jaws were designed and may be observed below in Figure 28. These jaws are made of aluminum to allow for some deformation while clamping the rough material finish of the raw DMLS wingtips. The jaws also utilize an elliptical cut which matches exactly the elliptical profile of the wingtips, thus allowing for increased contact and proper clamping capabilities.

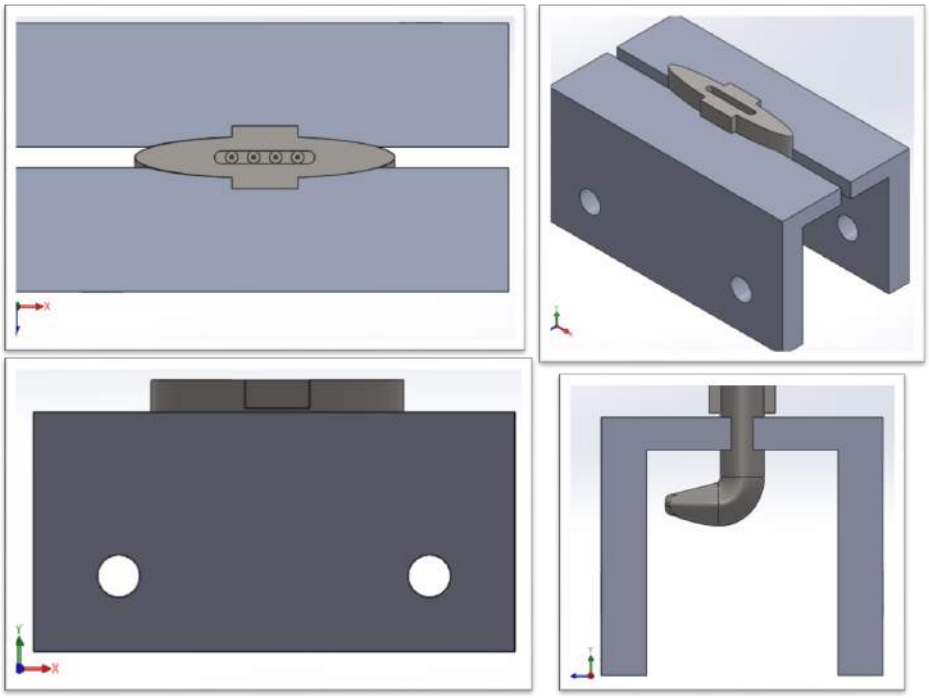

Figure 28: Soft Jaws. Top Left: Top View — Top Right: Isometric — Bottom Left: Front View — Bottom Right: Side View

In order to accurately complete the final machine processes it was also necessary to design the part such that it could easily be placed in a conventional CNC machine and be squared and zeroed on the X, Y, and Z axis. As seen from Figure 28, the elliptical profile of the wingtip was extended 0.4" beyond the necessary length, and a square extrusion 0.35" length was added to this section. This allowed a precision 0.05" spacer to be placed between the square extrusion and the top of the vise jaw, thus ensuring the part was square in the Z-axis and providing a reference for how much material to remove. The square extrusion also allowed for proper squaring, and zeroing of part in the X and Y axis of the machine. After the part was set in the machine, square and zero in all axis, the final machine processes could be performed.

7 Experimental Results and Discussion

7.1 Pressure Profiles

From the internal bores of the manufactured wingtip devices, experimental pressure profiles were obtained for each angle of attack (AoA) from 0 to 21 degrees, and from -12 to 21 degrees for the bidirectional reference EndCap device (Plain-Foil).

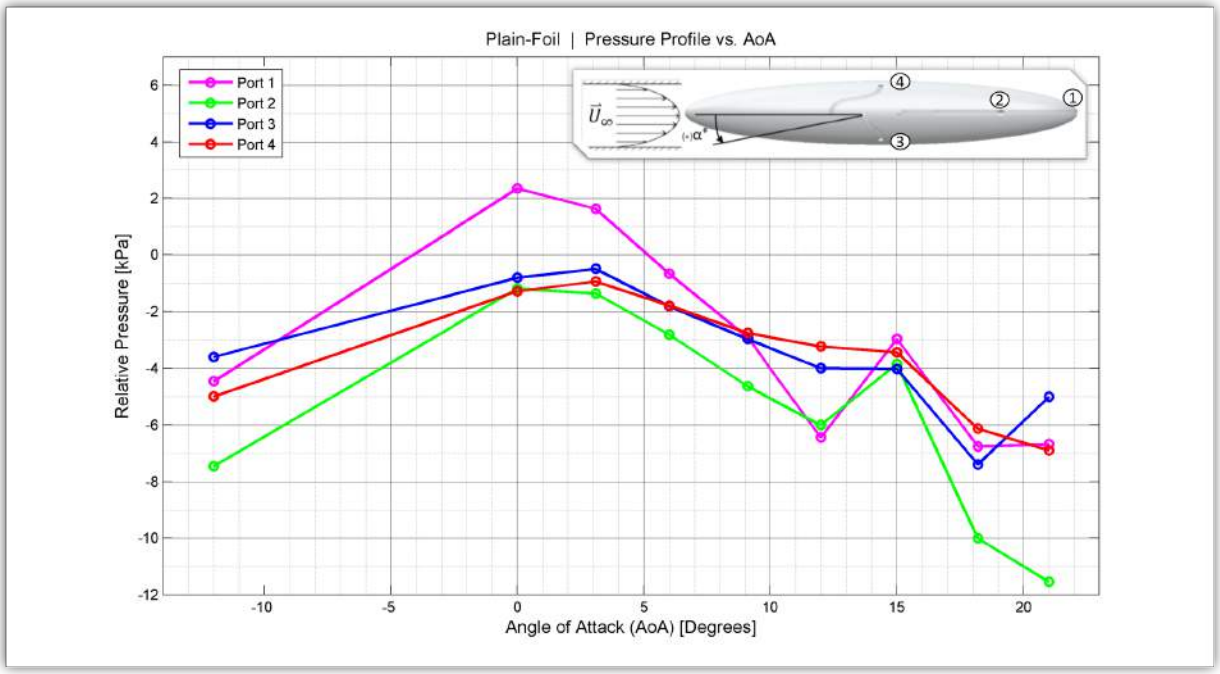

Figure 29: Pressure Profile of the Endcap. AoA measured positive-downwards. Port 4 on high pressure side — Port 3 on low pressure side — Port 1 & 2 located near trailing edge.

As seen from the above figure, with respect to the top and bottom pressure ports 4(blue) and 3(red) respectively, as the foil was flipped from negative to positive angles of attack the high and low pressure sides of the foil also flipped. This is to be expected and aids in justifying the accuracy of the pressure measurements. Also it may be observed that the difference in pressure between the top and bottom ports approaches zero at 0-degree AoA; the slight difference in measured pressure is likely due to the hydro-static pressure difference associated with the varying heights of the pressure locations. In future analysis the height of each of pressure port should be locally normalized about the origin of foil rotation to further increase the accuracy of results.

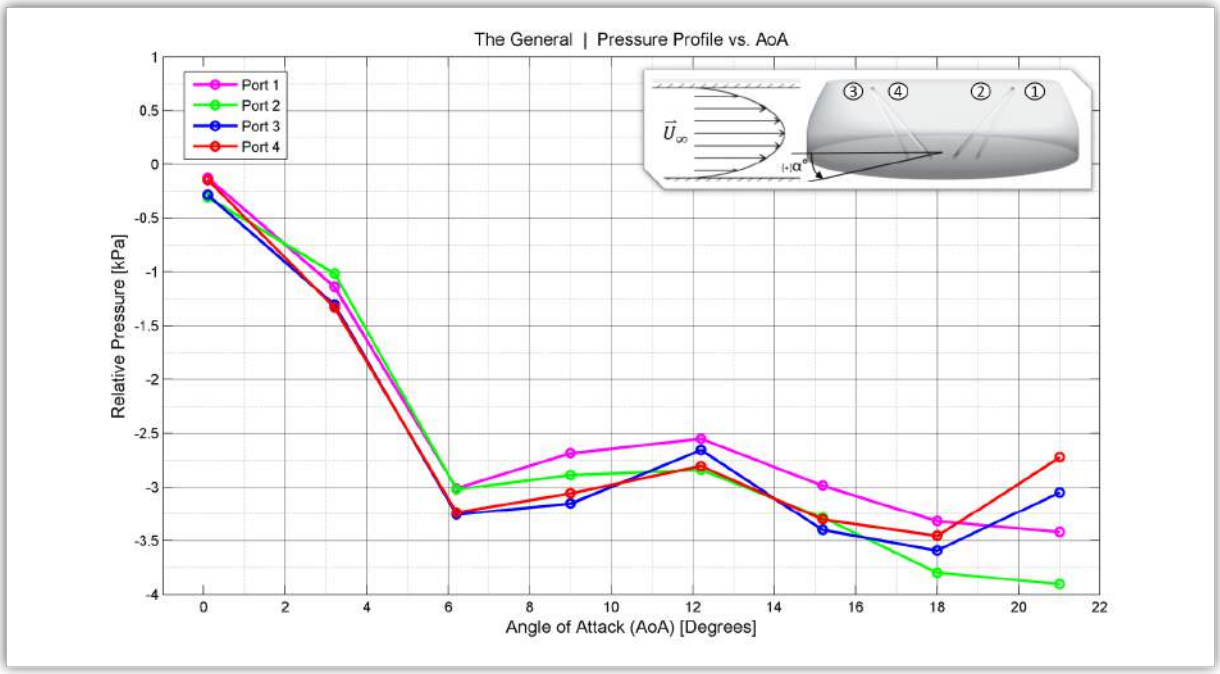

Figure 30: Pressure Profile of the general. AoA measured positive-downwards. Ports 2 & 3 on the Wingtip face coming out of the page — Ports 1 & 4 on the Wingtip face going into the page.

Referring to Figure 30: As expected from the theoretical design of *The General Wingtip Device*, the vertical geometric configuration of the wingtip aids in reducing the the pressure gradients experienced across the hydrofoil-wingtip. As discussed in the theory, minimizing the pressure gradients across a wingtip decreases the overall strength of wingtip vortices and aids in higher performance characteristics.

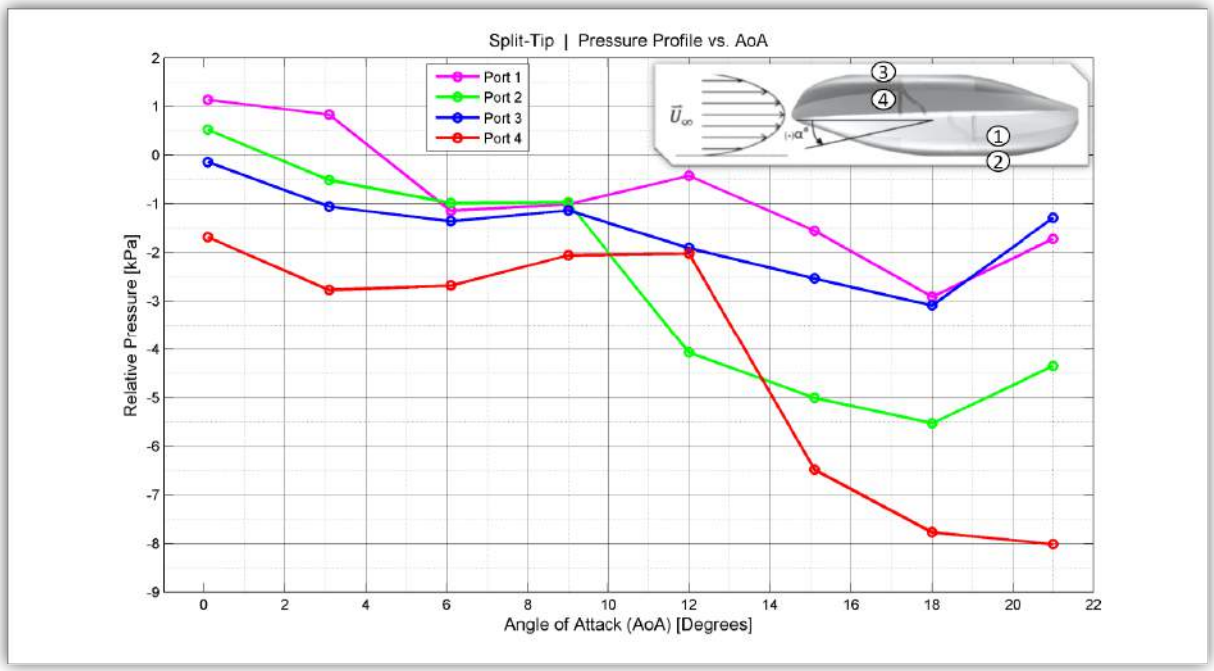

Figure 31: Pressure Profile of SplitTip.

Referring to Figure 31: The pressure differential across the upper and lower wingtip of *The SlitTip Wingtip Device* were much larger than those of *The EndCap* and *The General*; while this data does not support the effect of reducing wingtip vortices, the goal of this device is to produce vortical structures which crash into each other and help to negate their existence. This phenomena is difficult to measure given our pressure port locations and further analysis of lift and drag will be necessary to truly quantify the performance characteristics of this particular device.

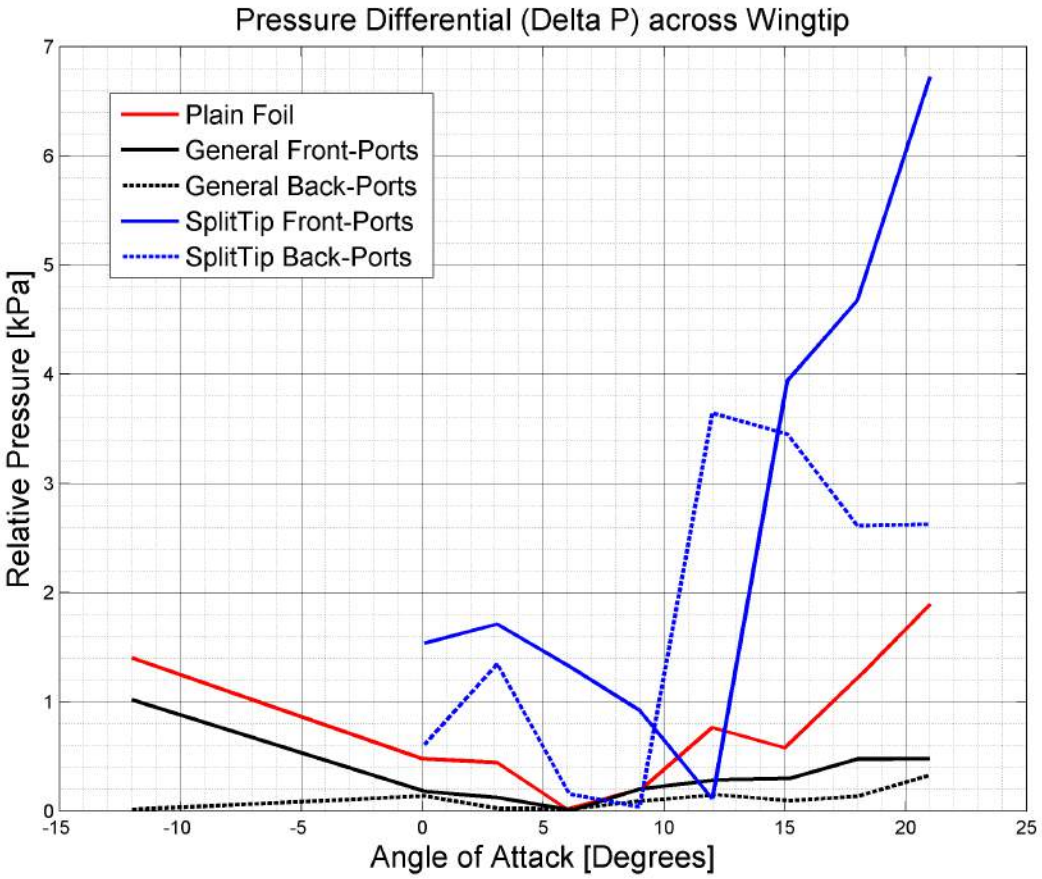

Figure 32: Pressure Differential about Wingtip Devices.

Figure 32 shown above displays the pressure differential across the wingtip device, as measured by the inline pressure ports on opposing sides of the wingtip device. As observed, *The General* produced the lowest pressure differentials across the wingtip, while the *The SlitTip* produced the largest pressure differentials across the wingtip. It may also be observed, as expected, that as the AoA increases the pressure experienced on the high pressure side of wingtip increases, while the pressure on the low pressure side decreases; in turn lending to increasing pressure differentials with increasing AoA.

7.2 Lift and Drag

In order to further analyze the performance characteristics of each wingtip device, the lift and drag of each device was measured experimentally at varying angles of attack. As seen below in Figure 33, the experimental data for each foil was plotted against the computational data for verification.

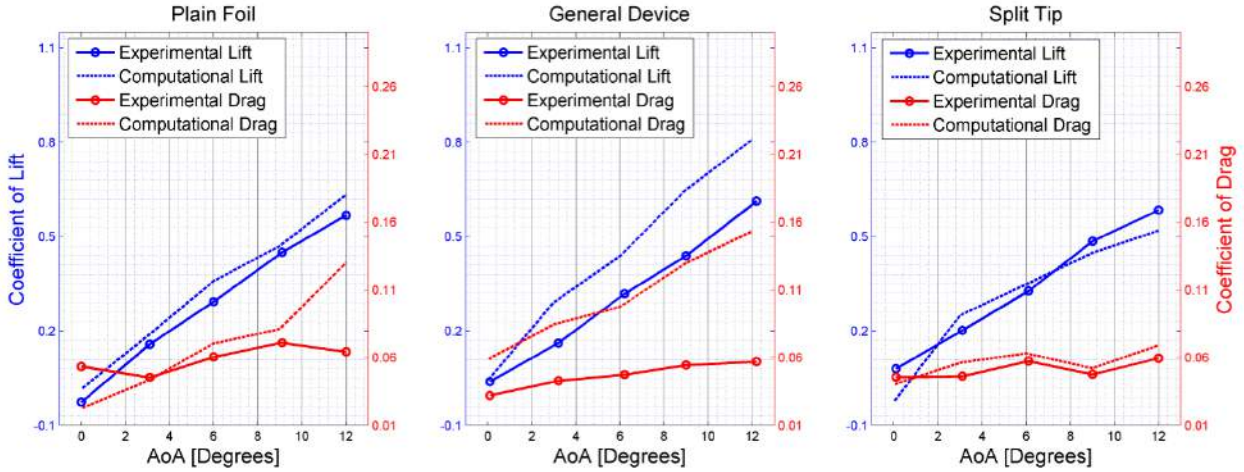

Figure 33: Lift and Drag of *The PlainFoil*, *The General*, and *The SplitTip*. The solid and dashed lines represent the experimental and computational data respectively. The blue and red lines represent the lift and drag measurements respectively.

As observed from the above Figure, the computational data matched very closely to the experimental data obtained for *The PlainFoil* and *The SplitTip*. There appears to be some discrepancy between the computational and experimental results of *The General*. Future experiments should test this device over multiple trials, both experimentally and computationally to confirm that the results converge each time. If they do not converge it will be apparent where the error is derived from. If the results of this test do converge it would require the simulation to be further advanced to accurately model the phenomena of this particular device.

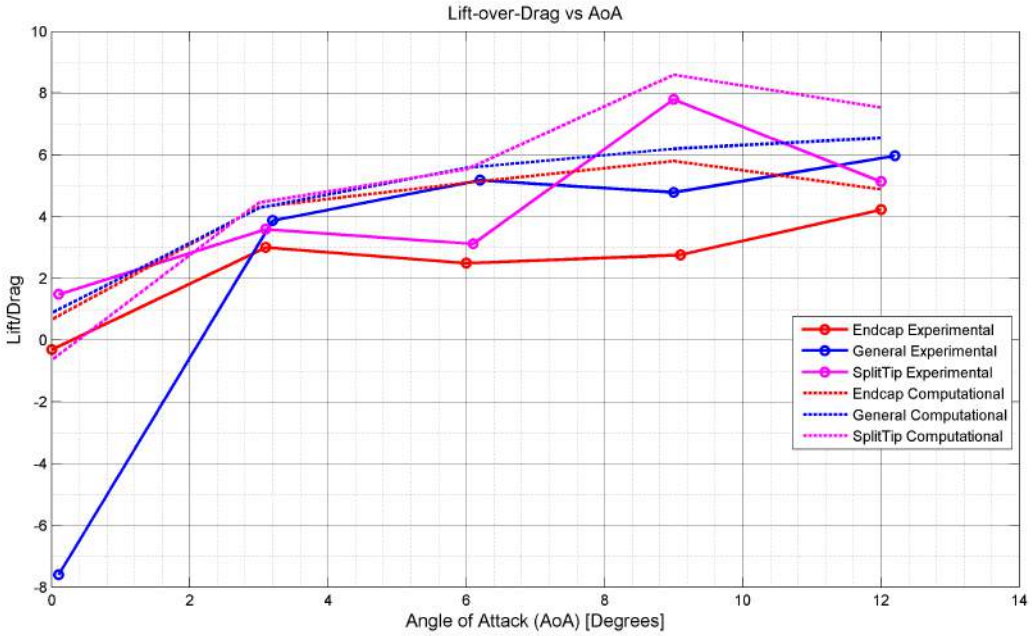

Figure 34: Lift over Drag for Each Wingtip Device. The solid and dashed lines represent the experimental and computational data respectively.

Figure 34 shown above provides a quantitative means of comparing the performance of each wingtip device as a ratio of lift over drag. Given the overarching goal of increasing lift and decreasing drag, the higher this ratio for each device the better the overall performance of that particular device. As displayed *The General* and *The SplitTip* consistently outperformed the basic reference foil, with the *The SplitTip* outperforming *The General* between 7 deg to 11 deg AoA.

Referring to Figure 34: The simulation measurement does not match exactly with the experimental data, however it is difficult to suggest that this is possible to do so with 100% accuracy. It should be noted however that the simulations were capable of producing accurate profiles of each device, even capturing which devices performed best and at which AoA the maximum performance occurs. The CFD simulation, in turn is a powerful means of rapidly quantifying the performance of a particular wingtip device prior to manufacturing.

8 Conclusion

Numerical and physical models were developed; capable of estimating and measuring the performance characteristics of MHK wingtip devices. The creation of computer generated geometries and HiCaT simulations, combined with a novel wingtip testing apparatus which exploits a variety of measurement capabilities, allows for the rapid development and optimization of MHK wingtip devices. This test-bed eliminates the need for extensive manufacturing and reduces the cost of developing wingtip devices. Manufacturing and experimenting of wingtip devices may in turn be limited to the best case, highest performance devices. Use of the HiCaT allows for validation of computational results and further quantification of complex phenomena, such as cavitition, vortical structure and strength, pressure profiles, and the effects of mass injection.

Through the developments of this project, two MHK wingtip devices with high performance characteristics were developed and validated through HiCaT experiments. Their geometric configurations attempt to avoid biofouling. *The General* device proved to greatly decrease the pressure differential across the wingtip, however due to the geometric configuration allowing this phenomena, blockage was increased and in turn the drag acting on the hydrofoil was seen to increase. *The SplitTip* device proved to have the best lift over drag performance characteristics and proved capable of operating at higher angles of attack; in turn this device is capable of producing substantially more power than a generic hydrofoil.

8.1 OpenFOAM - Future Development

Results of the *OpenFOAM* simulation showed agreement. However, there are a number of recommended steps to take in improving the numerical test-bed as listed below:

- Move to a transient solver - This will allow time dependent phenomena like vortex shedding to be seen in CFD. *cavitatingFoam* is recommended as it would also allow for cavitating vortices to be analyzed.
- Update the vorticity solver - Currently this solver shows max and min vorticity and also creates vorticity profiles for the entire simulation.
- Inlet velocity profile - Specifically actual vs uniform velocity profile.
- Create an algorithm that calculates circulation around a well defined vertex.
- Decrease mesh cell size and utilize super-computers.

8.2 HiCaT Experiments - Future Development

In order to further develop MHK turbine wingtips, there are multiple ways in which the experimental testing of these devices may be improved. The ability to test mass injection at varying pressures would be ideal for quantifying the effects of such phenomena. In order to achieve this, a high pressure pump with variable pressure output would be necessary for use at the HiCaT. During the experiments performed on the Wingtips described in this paper, it was attempted to inject liquid water directly from various ports on the HiCaT. However, it was determined that no matter where the location of the access port, high enough pressures were not achievable to produce significant mass injection rates and therefore the experimental results were inconclusive.

There also existed some difficulty in calibrating the HiCaT tunnel; particularly the drag calibration. It was also observed that after running the HiCaT at very high velocities, or cavitating flows, it was necessary to re-calibrate the force balance; this leads to additional experimental time requirements and decrease the repeatability of an experiment. Some of the data recorded for drag measurements appear to be erroneous as compared with other experiments. Future work to the HiCaT should focus on improving the measurement capabilities of force balance.

References

9 Bibliography

[1] Philip J. Pritchard. *Fox and McDonald's Introduction to Fluid Mechanics, 8th Edition*. John Wiley & Sons Inc, 2011.

[2] Phillip Eisenberg. *Cavitation*. Hydronautics Incorporated. Retrieved Nov 18, 2013.<http://web.mit.edu/hml/ncfmf/16CAV.pdf>.

[3] Ivaylo Nedyalkov. *Design of Contraction, Test Section, and Diffuser for a High-Speed Water Tunnel*. Thesis, Chalmers University of Technology. Gothenburg, Sweden 2012.

[4] Parker Hannin Corporation, Cleveland, OH. Parker O-Ring Handbook, 50th edition, 2007.

[5] Ismail Hameduddin. *Rotate vector(s) about an axis - rodrigues_rot (v, k, theta)*. Web. Matlab Central. Jan 2012.

[6] Andrew French. *Gravity Simulator - ellipse (xc, yc, a, b, N)*. Web. Matlab Central. Jan 2013.

[7] "Wake Vortex Study at Wallops Island." NASA Langley Research Center. Web. Wikipedia. 4 May 1990.

[8] "The Wind Turbine Albedo Effect." Anthony Watts. Watts Up With That?. Web. 28 Apr. 2011.

[9] "DGLR E.V. - Aeronautics Days 2006." DGLR E.V. - Aeronautics Days 2006. N.p., n.d. Web. 17 Apr. 2014.

[10] Gagnon, M.Sc. Lousi, and Dr. Mar J. Richard. Parallel CFD of a Prototype Car with OpenFOAM. Tech. Gothenburg, Sweden: Chalmers, 2010. Print.

[11] "UK: DP Barge Set to Revolutionise Tidal Energy Installation Challenge - Alstom Tidal Turbine" Alstom.com. Web. 15 Feb 2013.

[12] "Atlantis Deploys 1 MW..." SubSeaWorldNews. Web. 15 Feb 2013.

10 Appendices

10.1 Appendix A - OpenFOAM Images

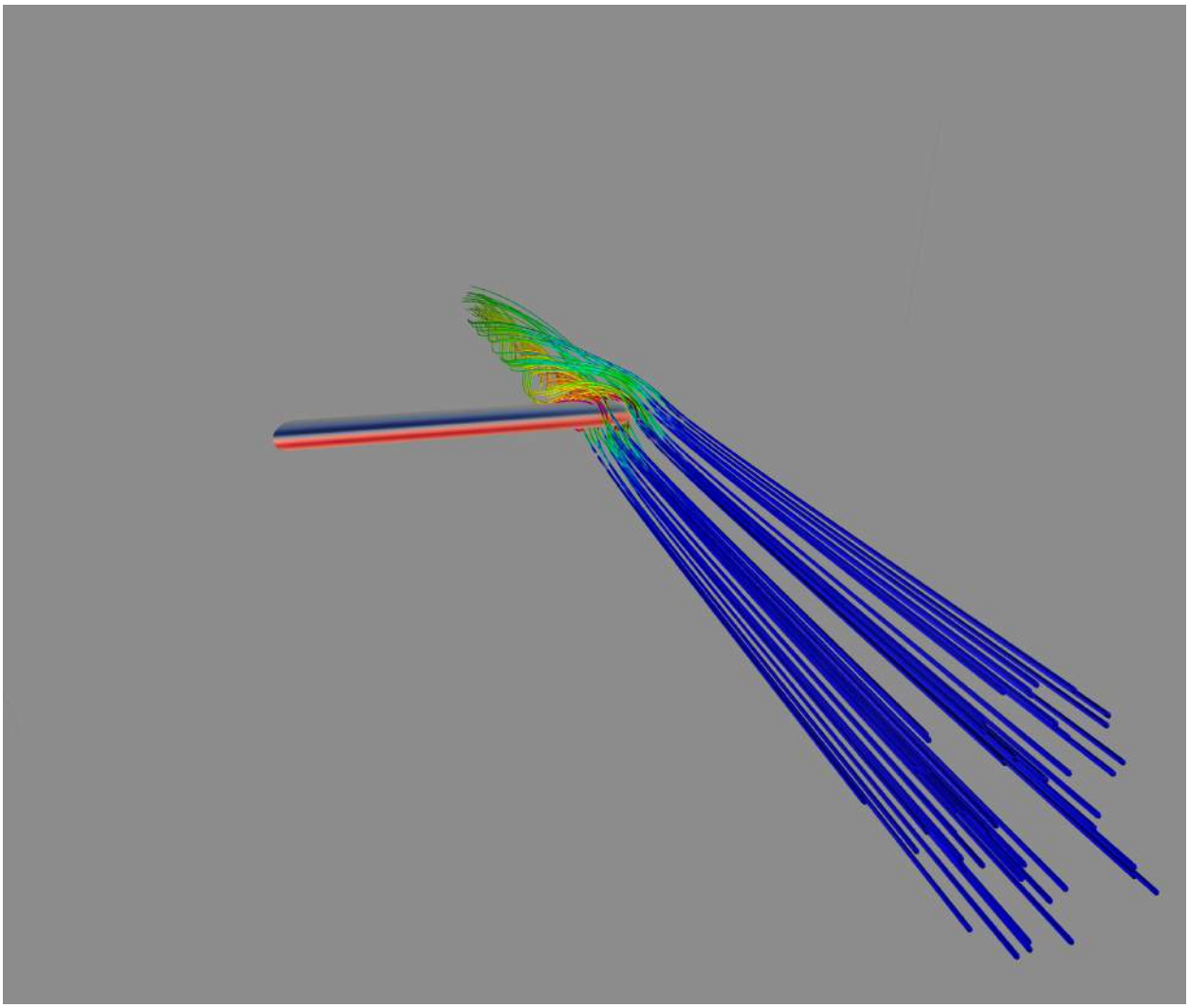

Figure 35: Pressure profile shown on Plain Foil from the left and vorticity magnitude shown on the streamlines.

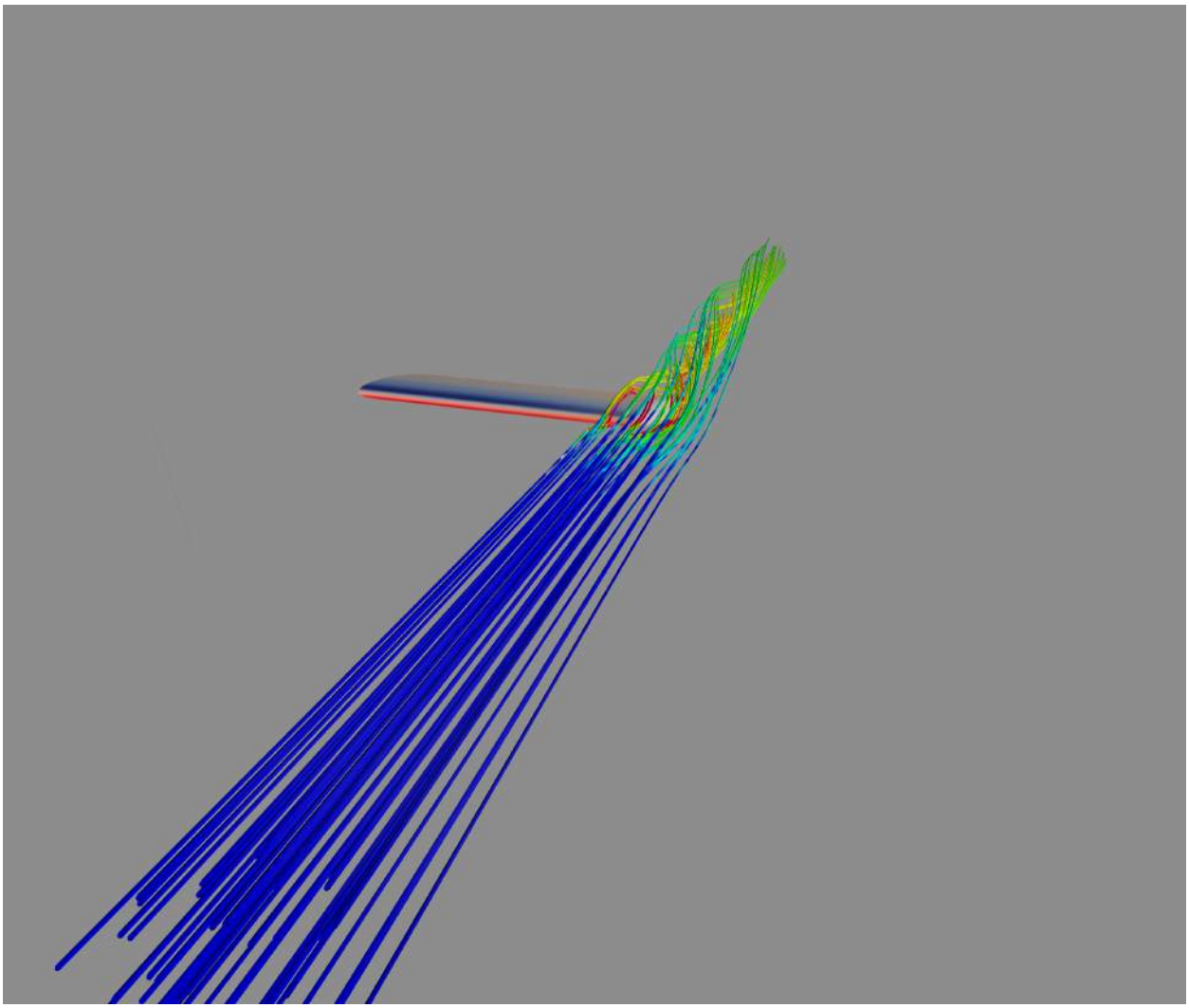

Figure 36: Pressure profile shown on Plain Foil from the right and vorticity magnitude shown on the streamlines.

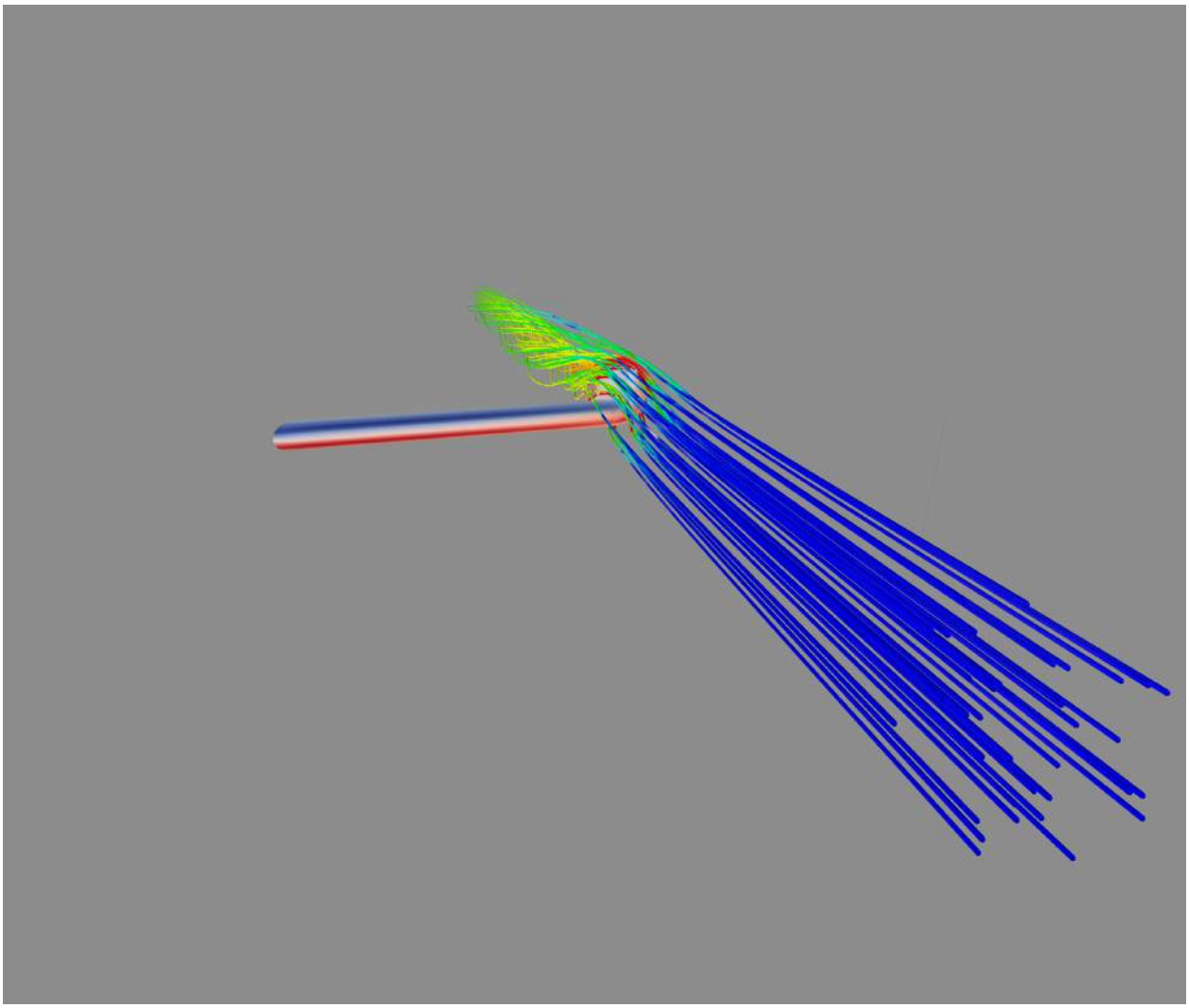

Figure 37: Pressure profile shown on The General from the left and vorticity magnitude shown on the streamlines.

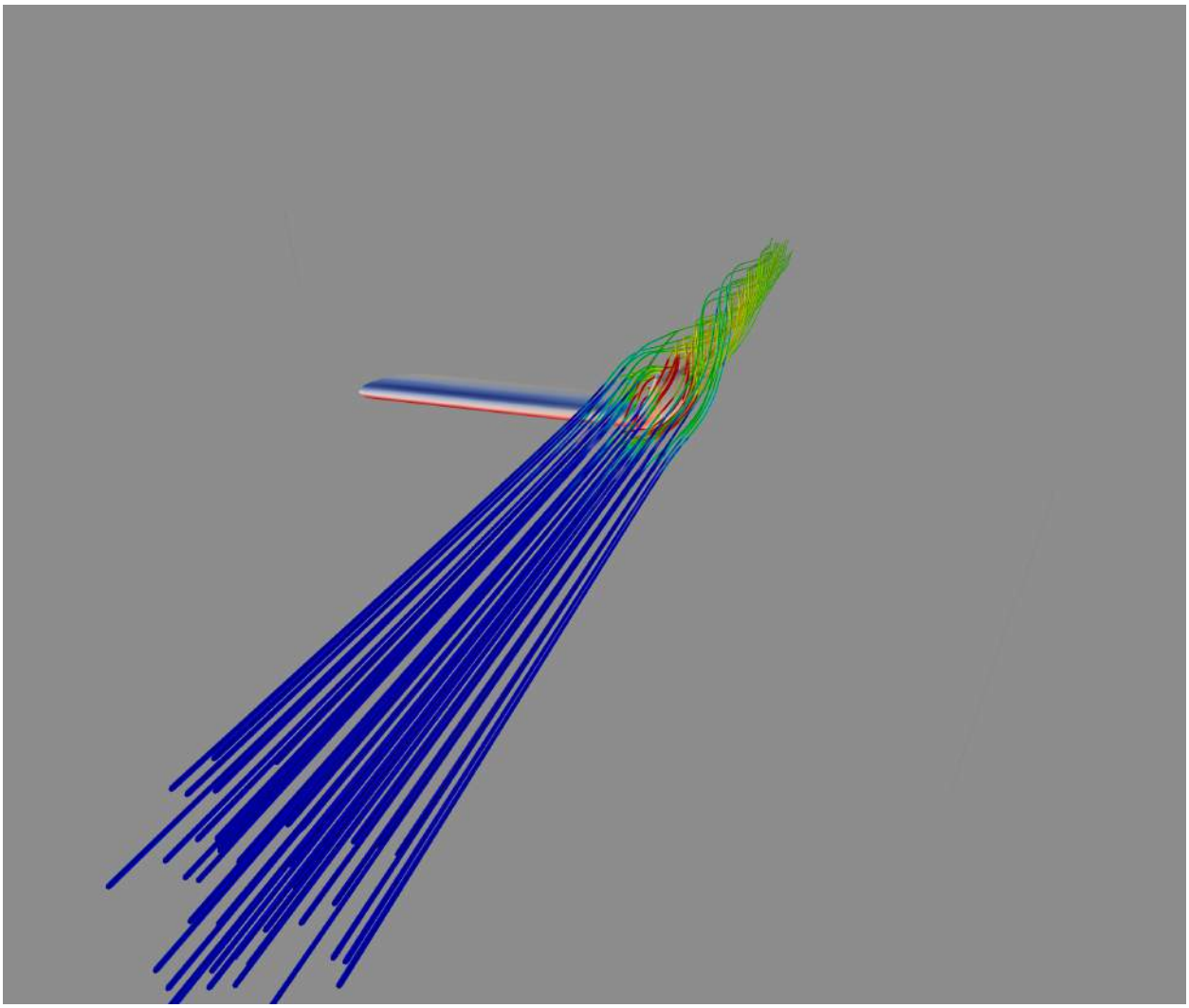

Figure 38: Pressure profile shown on The General from the right and vorticity magnitude shown on the streamlines.

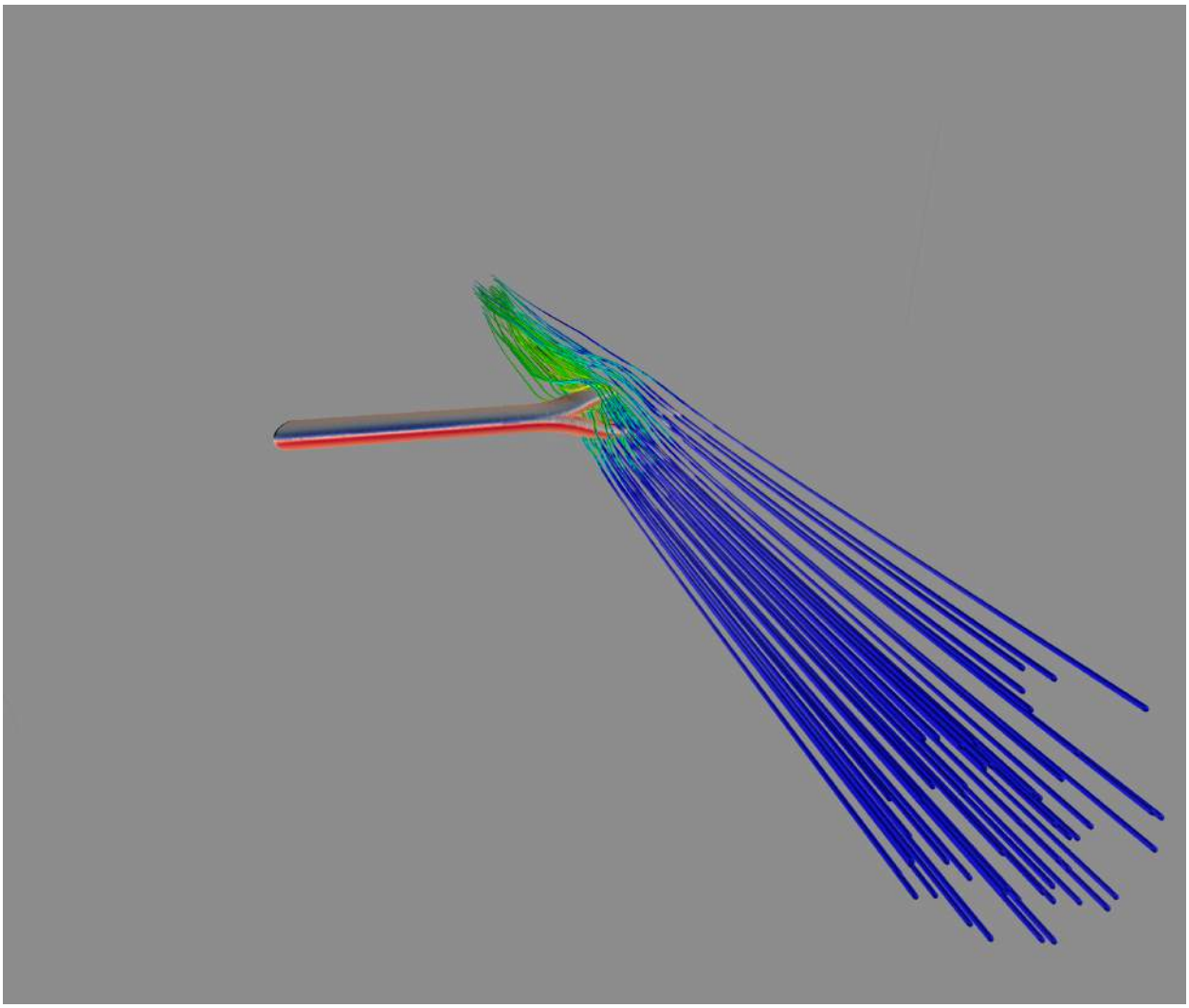

Figure 39: Pressure profile shown on SplitTip from the left and vorticity magnitude shown on the streamlines.

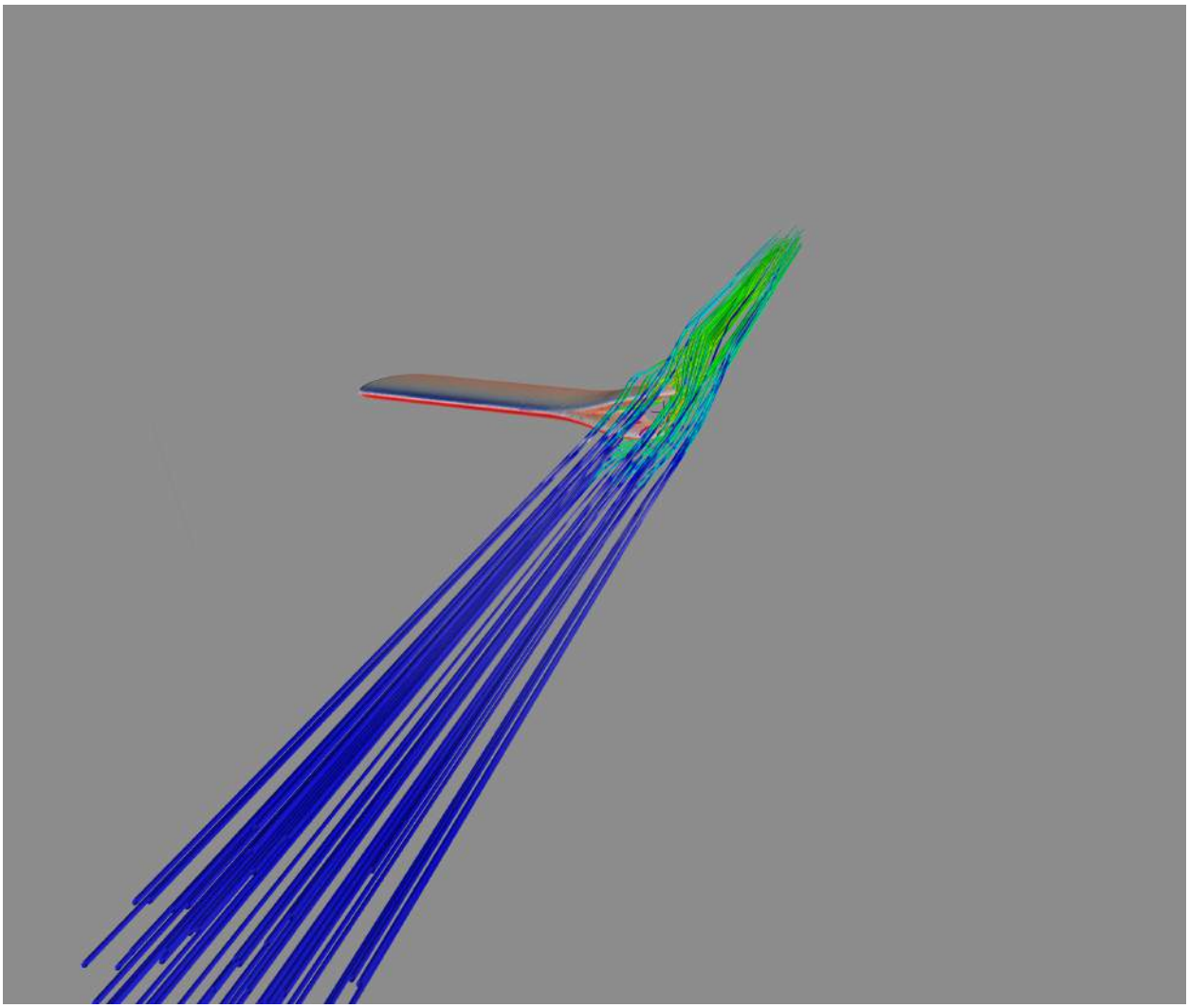

Figure 40: Pressure profile shown on SplitTip from the right and vorticity magnitude shown on the streamlines.

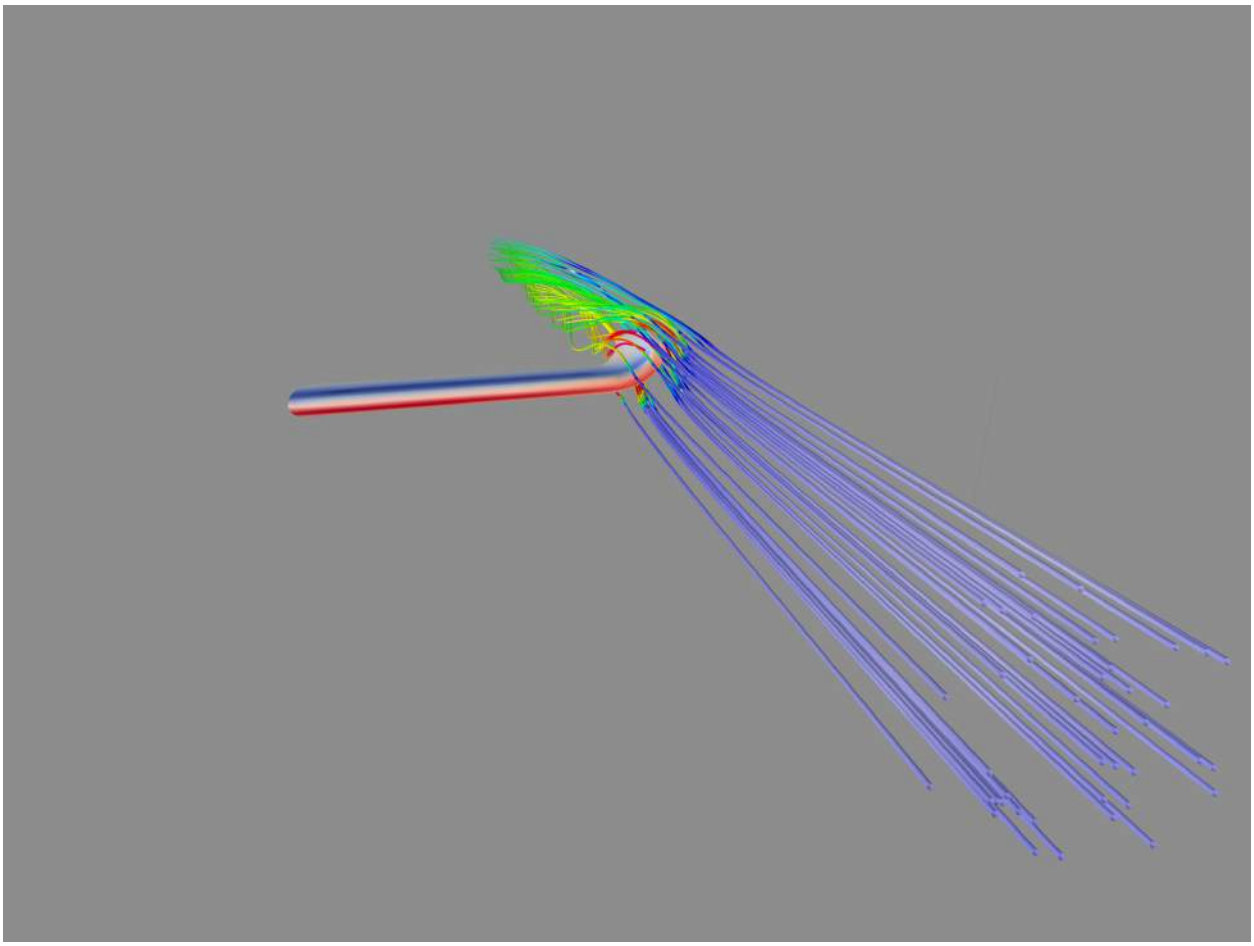

Figure 41: Pressure profile shown on Simple Curve from the left and vorticity magnitude shown on the streamlines.

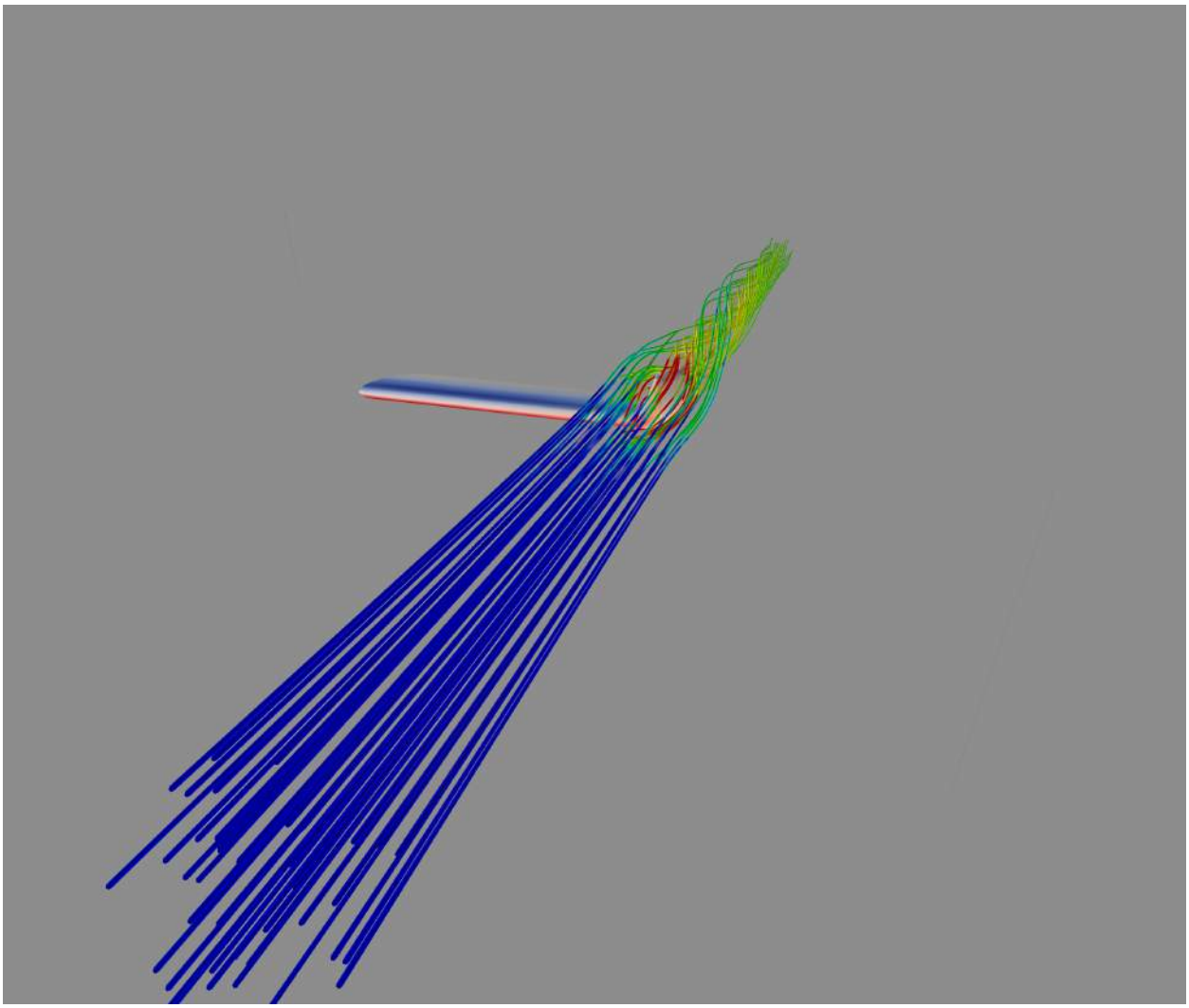

Figure 42: Pressure profile shown on Simple Curve from the right and vorticity magnitude shown on the streamlines.

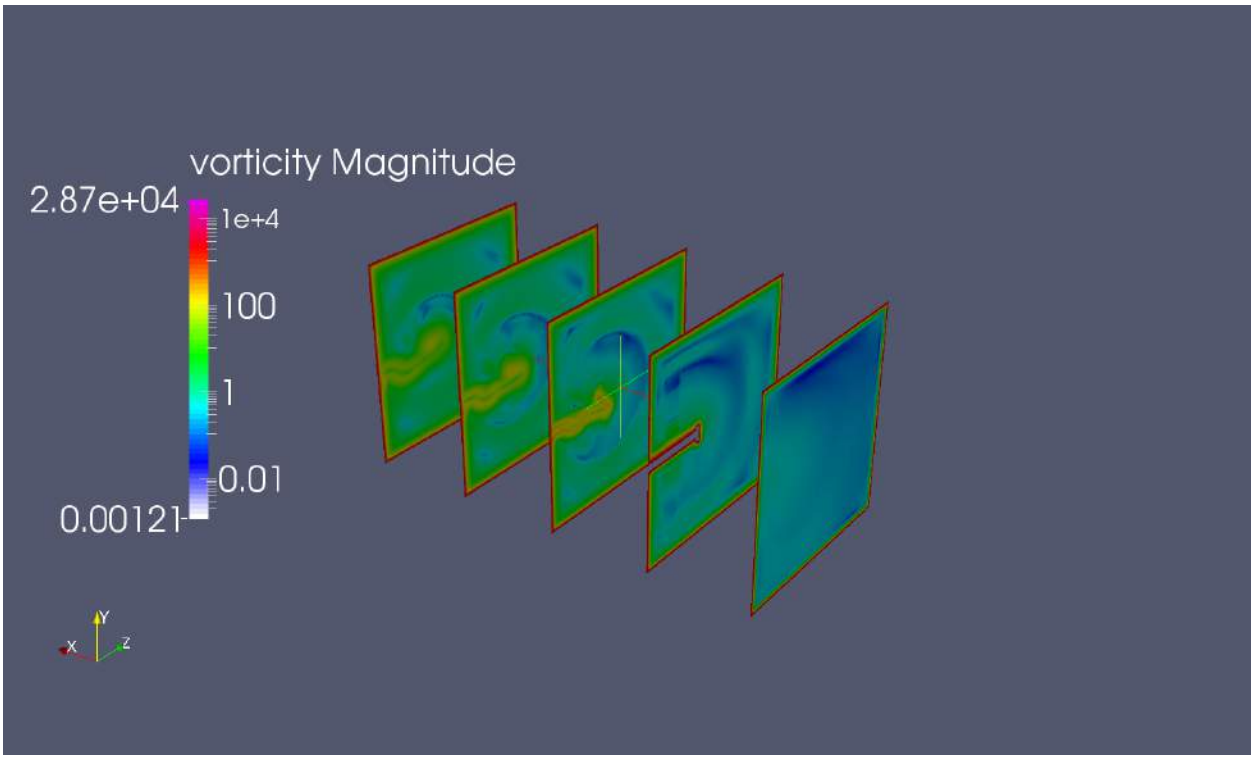

Figure 43: Slices showing vorticity on the V-Back.

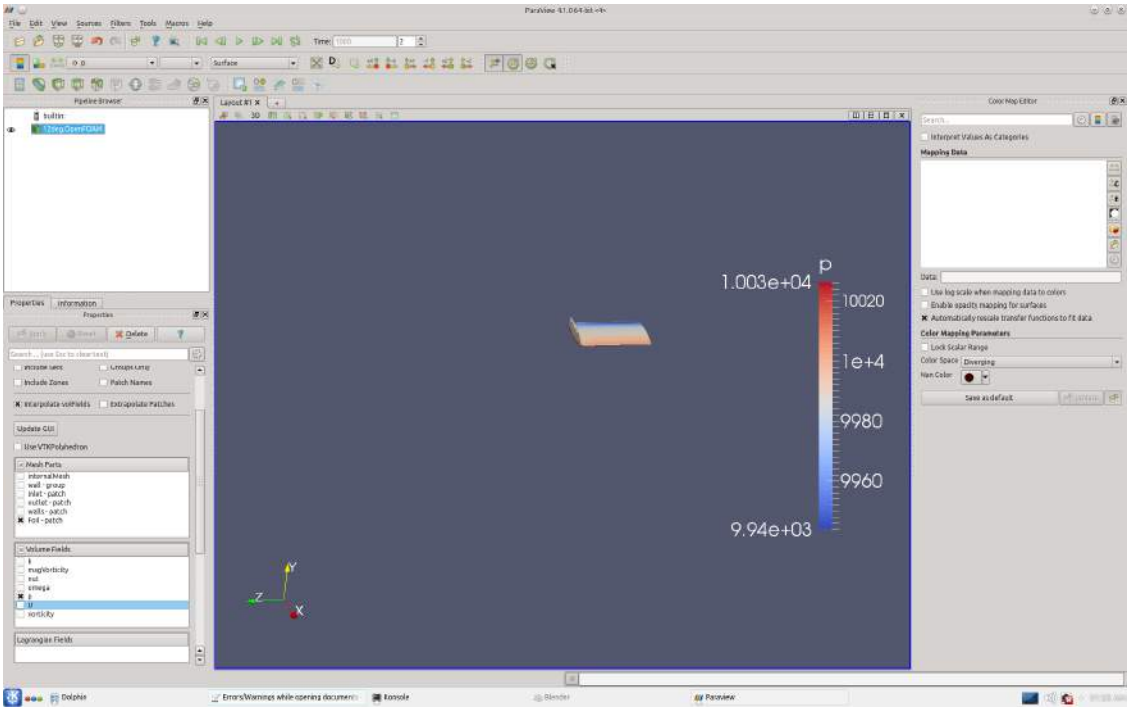

Figure 44: Pressure Profile on The General as seen in *ParaView*.

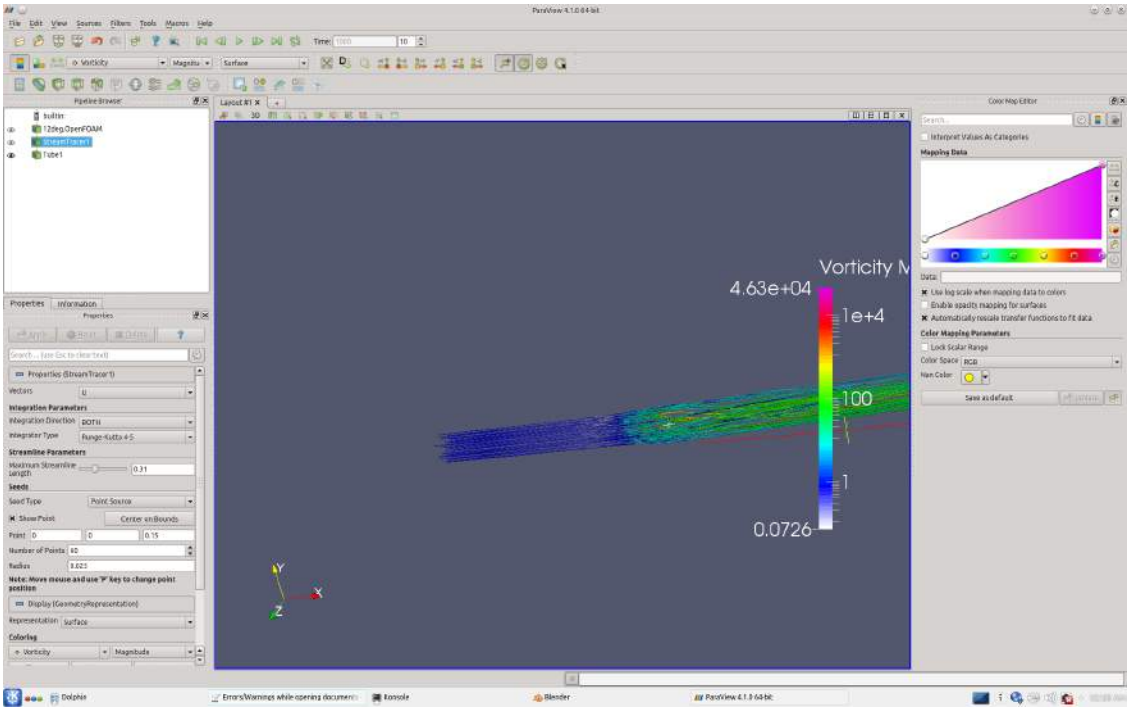

Figure 45: Vorticity streamlines from the SplitTip as seen in *ParaView*.

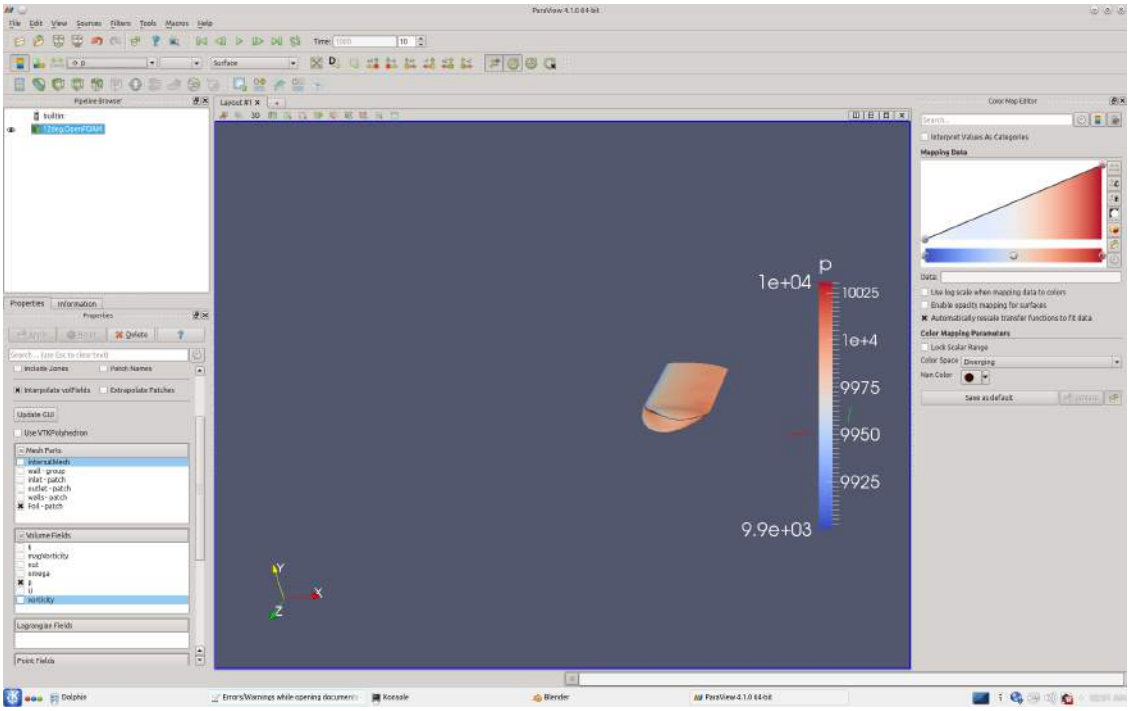

Figure 46: Pressure profile on the SplitTip as seen in *ParaView*.

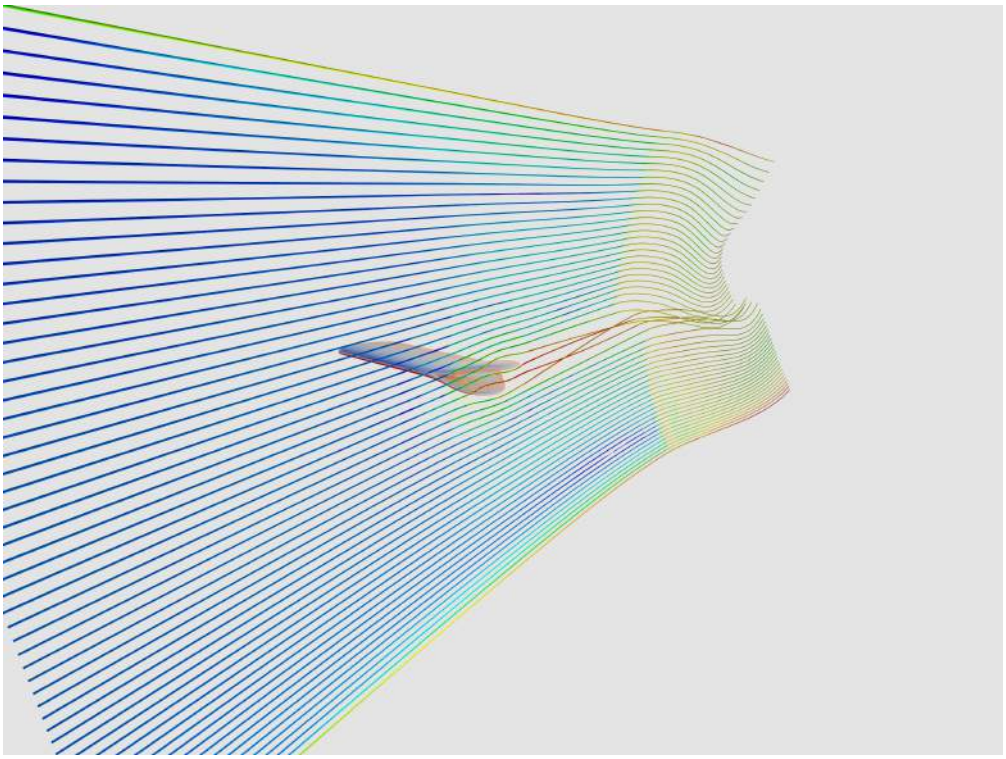

Figure 47: SplitTip vorticity profile from the side from *Blender*.

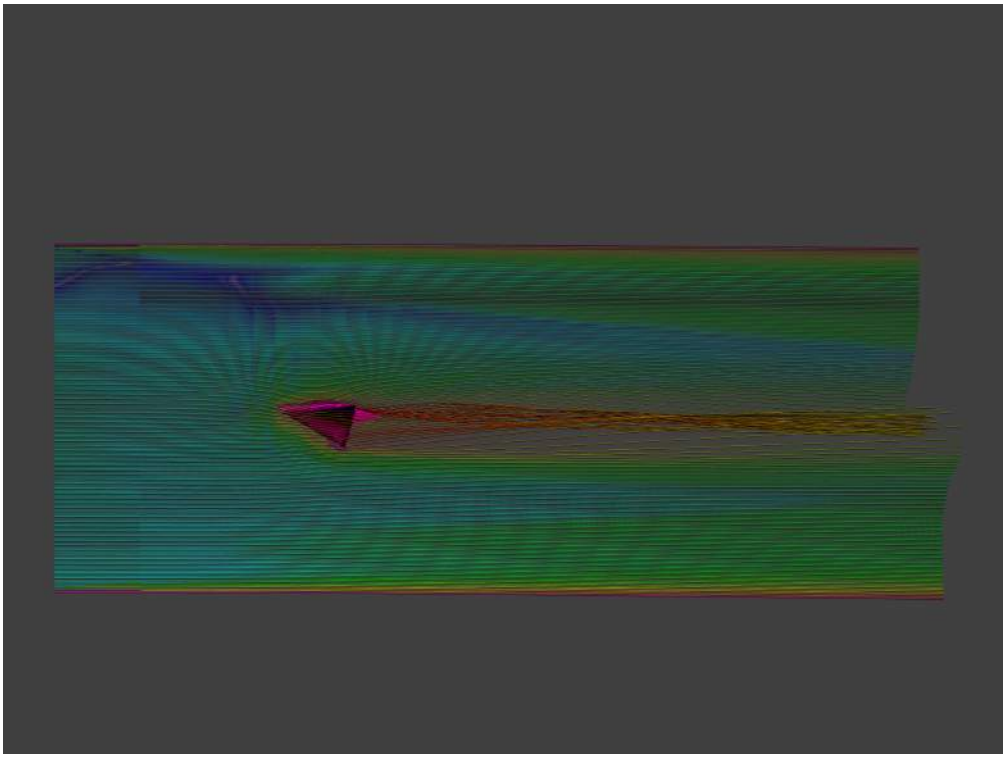

Figure 48: Streamline visualizations of vorticity magnitude on the concept tip, V-Back.

10.2 Appendix B - OpenFOAM Case Directory

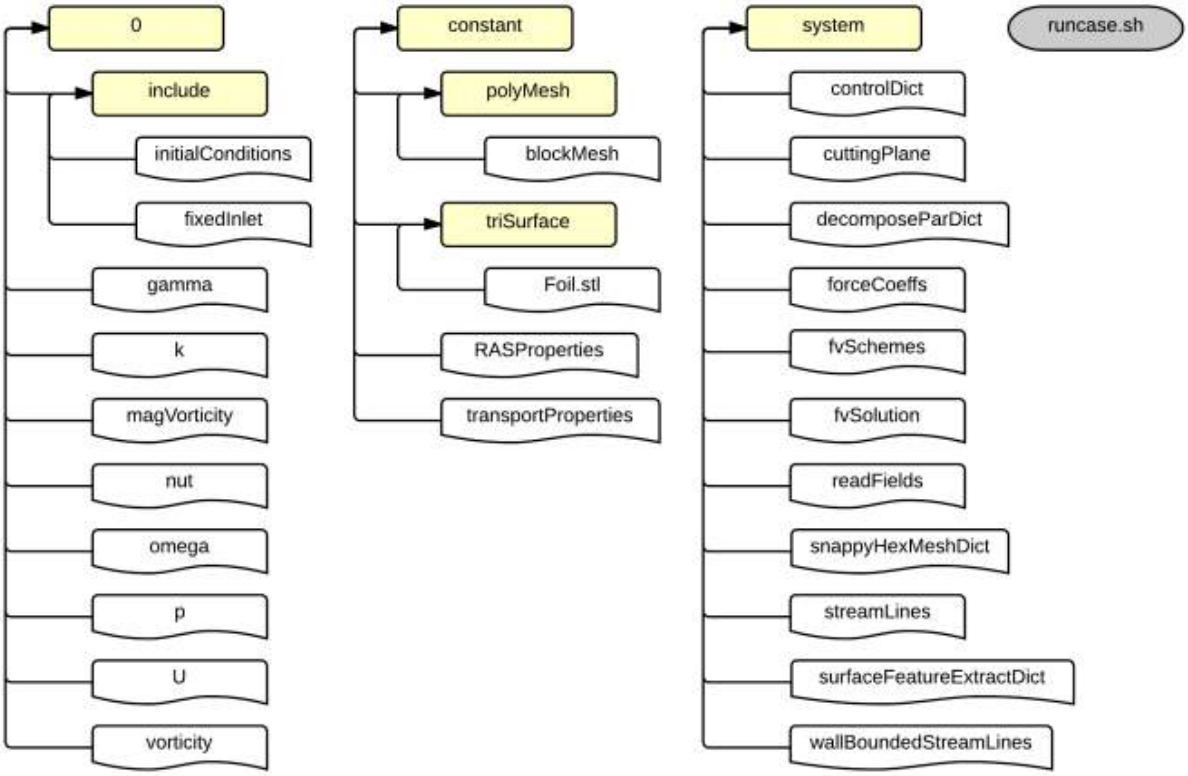

Figure 49: Case Directory breakdown.

A zip file of the OpenFOAM HiCaT Simulation case directory is available on Dropbox at https://db.tt/Pj8HaC9t

10.3 Appendix C - OpenFOAM User Guide

A short guide to running the HiCaT simulation

Pre-Simulation:
OpenFOAM must be installed
OpenMPI must be installed for parallel processing
ParaView is needed to visualize data

Directions:
Delete all files in constant/triSurfave
Copy STL here
rename file to "Foil.stl"

There are two options for running the simulation There is a stable 1-core version and an unstable parallel processing version:

Option 1 - single_core.sh
in terminal navigate to case directory

```
run "chmod +x single_core.sh"
run "./single_core.sh"
```

Option 2 - parallel_processing.sh
in terminal navigate to case directory

```
run "chmod +x parallel_processing.sh"
run "./parallel_processing.sh"
```

Notes and Recommendations: The advantage of parallel processing is in the speed of completion. The number or cores that the processing is split between can give you a rough estimate of time. Take the time it took for the single core simulation to run and divide by the number or cores time about 95% parallel process efficiency. This should be used when running single tests when time is important. The problem with parallel processing (which utilizes MPI) seems to be due to the moving of the mesh between cores. This typically causes *snappyHexMesh* to fail.

The settings for parallel processing are found in /system/decomposeParDict Determine the number of cores for a job to be run on. The most stable decomposition method was found to be "simple" however, the "ptscotch" method is known to be faster. Would recommend moving to this method.

Make sure to addjust the coefficients found next to "n" to work for the number of cores being used (multiply the three numbers to equal number of cores).

In /system/controlDict adjust end time and write intervals as desired. Note that time is actually just number of iterations in the case of simpleFoam. When moving to an unsteady solver, this will no longer be the case. It is recommended in early stages to use smaller write intervals to do a convergence test (no convergence study was done but many test converged before 2000 iterations). For optimization and AOA tests, it is recommended that the write interval and end time are set to the same value. This will save hard drive space.

writeControl is set to adjustableRunTime so that each simulation will stop after it has reached convergence.

If moving to an unsteady time dependent solver it is recommended that simpleFoam be used to get the simulation to a reasonable convergence, and then using the time dependent solver afterwards. This will reduce computation time.

Initial Conditions are set in 0/include/intialConditions

blockMesh

defined in constant/polyMesh The tunnel is defined by 8 points at the top of the file. Under the blocks section hex(0 1 2 3 4 5 6 7) defines the tunnel and the next set of numbers defines the number of divisions per dimension. a 2mm block size was used, but is recommended to decrease this once simulations are being sent out to servers. Decreasing size will allow for more phenomina to be visable.

snappyHexMesh

Changing the number of levels will change the meshing of the foil surface. 2 levels means that the foil will be resolved to half the dimensions of the blockMesh dimensions. 3 levels will be one fourth and so on.

On Crashes: *OpenFOAM* puts out very ugly crash reports. This can be overwhelming. Take your time in reading the output after a crash. The source of the error will be noted. Find the point where the simulation crashed (there should be good output up to the point of failure and then a large amount of failure notation). The error that caused the failure will be close to this point. If foamJob (MPI) is failing, make sure that *snappyHexMesh* ran correctly. If it did, re-run *decomposePar* as it may have failed. If failures continue, run on a single-core to make sure the case is stable.